Journal of Structural Geology 33 (2011) 1359–1377

Contents lists available at ScienceDirect

Journal of Structural Geology

journal homepage: www.elsevier.com/locate/jsg

Microtectonic and geochemical characterization of thrusting in a foreland basin: Example of the South-Pyrenean orogenic wedge (Spain)

B. Lacroix [a,*], M. Buatier [a], P. Labaume [b], A. Travé [c], M. Dubois [d], D. Charpentier [a], S. Ventalon [e], D. Convert-Gaubier [a]

[a] Chrono-Environnement, UMR 6249, Université de Franche Comté, 16 route de Gray, 25000 Besançon, France
[b] Géosciences Montpellier, UMR 5243, Université Montpellier 2, 34095 Montpellier, France
[c] Departament de Geoquímica, Petrologia i Prospecció Geològica, Universitat de Barcelona, 08028 Barcelona, Spain
[d] LGCgE, EA 45 15 – UFR des Sciences de la Terre, Université Lille 1, 59655 Villeneuve d'Ascq cedex, France
[e] FRE CNRS 3298 Géosystèmes, Université Lille 1, 59655 Villeneuve d'Ascq cedex, France

ARTICLE INFO

Article history:
Received 7 March 2011
Received in revised form
30 May 2011
Accepted 17 June 2011
Available online 25 June 2011

Keywords:
Fluid-rock interaction
Stable isotope
Fluid inclusion
Pressure solution cleavage
Thrust-and-fold belt

ABSTRACT

In orogenic systems, thrust faults play a major role in stacking different tectonic units and may act as conduits for the expulsion of large amounts of fluid of different origins (metamorphic, diagenetic, meteoric). This study focuses on the Monte Perdido thrust unit emplaced in the Paleogene Jaca thrust-sheet-top basin, in the SW-central Pyrenees. We aim to decipher the mechanisms and P-T conditions of deformation in fault zones and characterize the related fluid involvement, through combined microstructural, geochemical and microthermometry analyses. Two thrust faults cutting platform limestones, marls and siliciclastic turbidites of the lower part of the basin-fill (Paleocene–lower Eocene) have been studied. The fault zones are characterized by metre-thick shear zones with highly deformed, foliated clay-rich sediments. Foliation is underlined by preferentially oriented phyllosilicates. Several generations of shear and extension calcite, quartz and chlorite-bearing veins attest to fluid-rock interactions during a multi-stage deformation. Microstructural observations and stable isotope analyses on calcite from veins and host sediments suggest that deformation was aseismic and dominated by diffusive mass transfer from pressure solution sites along cleavage and stylolites to the precipitation sites in veins, with mineralizing fluids in equilibrium with the host sediments. Our results suggest an essentially closed hydrologic system, and imply the absence of significant fluid flow along the studied fault zones. Microthermometric study on fluid inclusions present in calcite and quartz veins, and calcite-quartz oxygen isotopic fractionation determined for the first generation shear veins, allow a geothermal gradient of 34 °C/km to be estimated. Analytical results demonstrate an evolution of the fault zones in three stages. The first stage was related to the emplacement of the Monte Perdido thrust unit during the middle Eocene at a temperature of ~208 °C and a burial depth of ~5.7 km. The second stage corresponds to a fault reactivation at a temperature of ~240 °C and a burial depth of ~6.5 km. The latter deformation may have been related to folding of the Monte Perdido thrust unit during the emplacement of the underlying Gavarnie thrust unit during the late Eocene–early Oligocene, with deeper burial resulting from aggradation of the thrust-sheet-top basin-fill. The last event corresponds to the formation of a dilatant vein system likely related to the exhumation of the massif.

1. Introduction

During the last two decades, many studies have shown that physical properties of faults, in particular porosity and permeability, change during deformation processes (*e.g.* Zhang and Tullis, 1998; Fisher and Knipe, 2001; Zhang et al., 2001). As a result, active faults may act as major pathways for fluid flow through the crust and at different P-T conditions. During the formation of orogenic belts, significant fluid flow from different sources (*i.e.* sediment compaction, meteoritic water, metamorphic dehydration water or magmatic fluids) can migrate through thrust faults towards the foreland and participate in fluid-rock interactions, alteration of wall rock compositions, and precipitation of new mineral phases in veins (*e.g.* Marquer and Burkhard, 1992; Travé et al., 1997; Kenis

* Corresponding author. Tel.: +33(0)381665061; fax: +33(0)381666568.
E-mail address: brice.lacroix@univ-fcomte.fr (B. Lacroix).

0191-8141/$ – see front matter © 2011 Elsevier Ltd. All rights reserved.
doi:10.1016/j.jsg.2011.06.006

et al., 2000; Séjourné et al., 2005; Barker et al., 2006; Caja et al., 2006; Vilasi et al., 2009).

Due to their economic interest, in particular oil exploration, much recent work has focused on the study of fluid flow in thrust-and-fold belts and related foreland basins such as those of Albania (Vilasi et al., 2006, 2009; Lacombe et al., 2009), Mexico (Ferket et al., 2000, 2003, 2006; Roure et al., 2009), Pyrenees (Travé et al., 1997, 1998, 2007; Buatier et al., 1997) and Wyoming (Wiltschko et al., 2009). However, fluid-rock interactions and fluid sources often remain difficult to interpret, a major challenge being the determination of the P-T conditions of thrust activity. For this purpose, mineral precipitation along fractures potentially provide a powerful tool to characterize fluid-rock interactions and the fluid composition that flowed through the faults, but also to determine the P-T conditions of precipitation.

The present study focuses on the northern part of the South-Pyrenean thrust-and-fold belt (Figs. 1 and 2), where stratigraphic, structural, and temperature conditions are relatively well constrained (*e.g.* Séguret, 1972; Mutti et al., 1988; Holl and Anastasio, 1995; Remacha et al., 2003). Different authors investigated fluid flow and fluid-rock interactions related to thrusting in this area. In the southern part of the Axial Zone, Grant (1990), McCaig et al. (1995, 2000) and Henderson and McCaig (1996) characterized fluid flow under greenschist facies conditions along the Gavarnie basement thrust. Rye and Bradbury (1988) studied fluid-rock interactions in veins from the Upper Cretaceous limestone cover. In the Ainsa basin, Buatier et al. (1997) and Travé et al. (1997, 1998, 2007) characterized fluid behaviour in the lower Eocene foreland basin fill at the front of the Cotiella nappe. Although these studies characterized fluid-rock interactions, fluid sources and

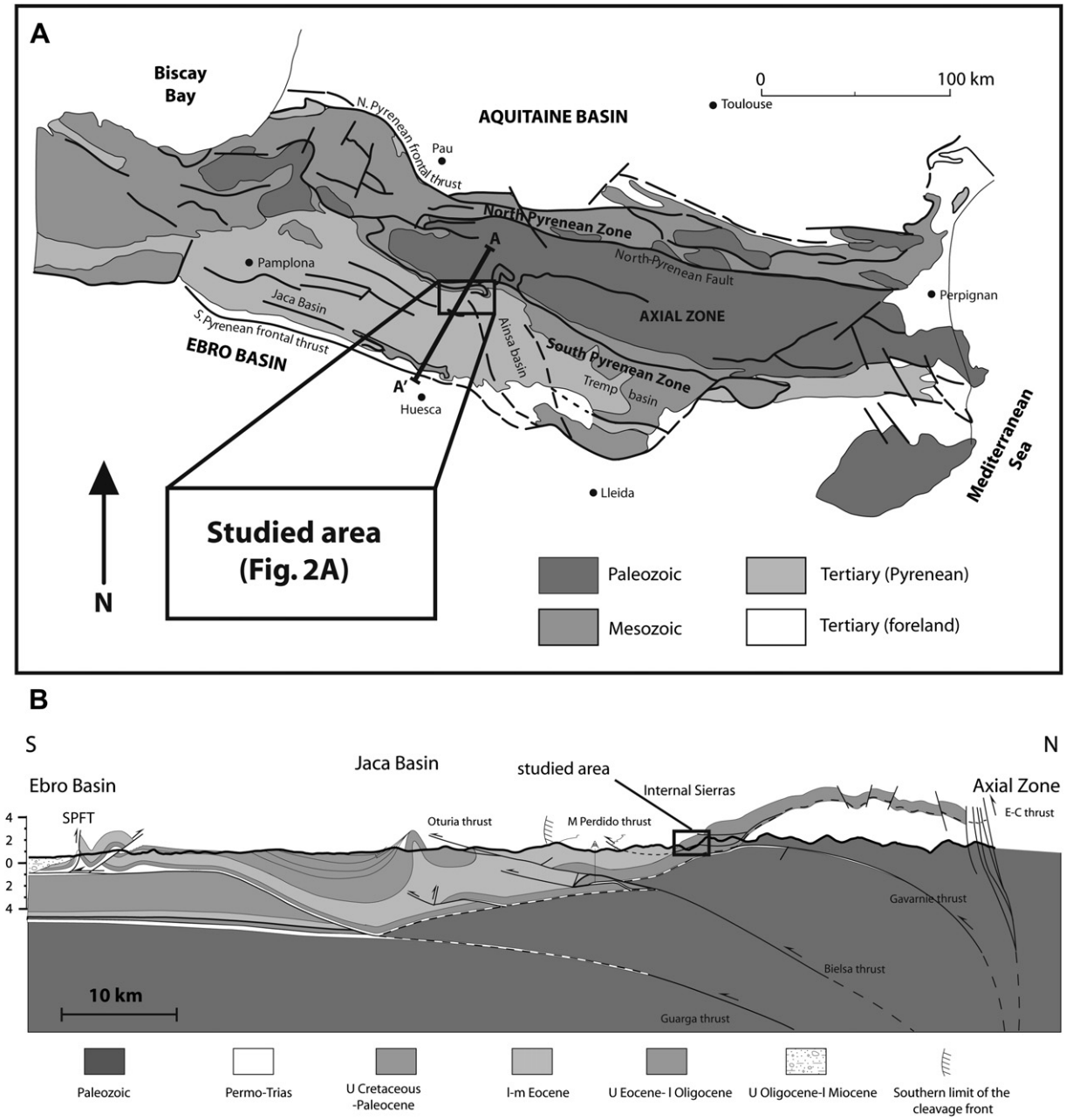

Fig. 1. A. Structural map of the Pyrenees with the location of the study area. B. Cross-section of the Axial Zone and South-Pyrenean Zone (Jaca thrust-sheet-top basin) modified from Meresse (2010) (location: line in A).

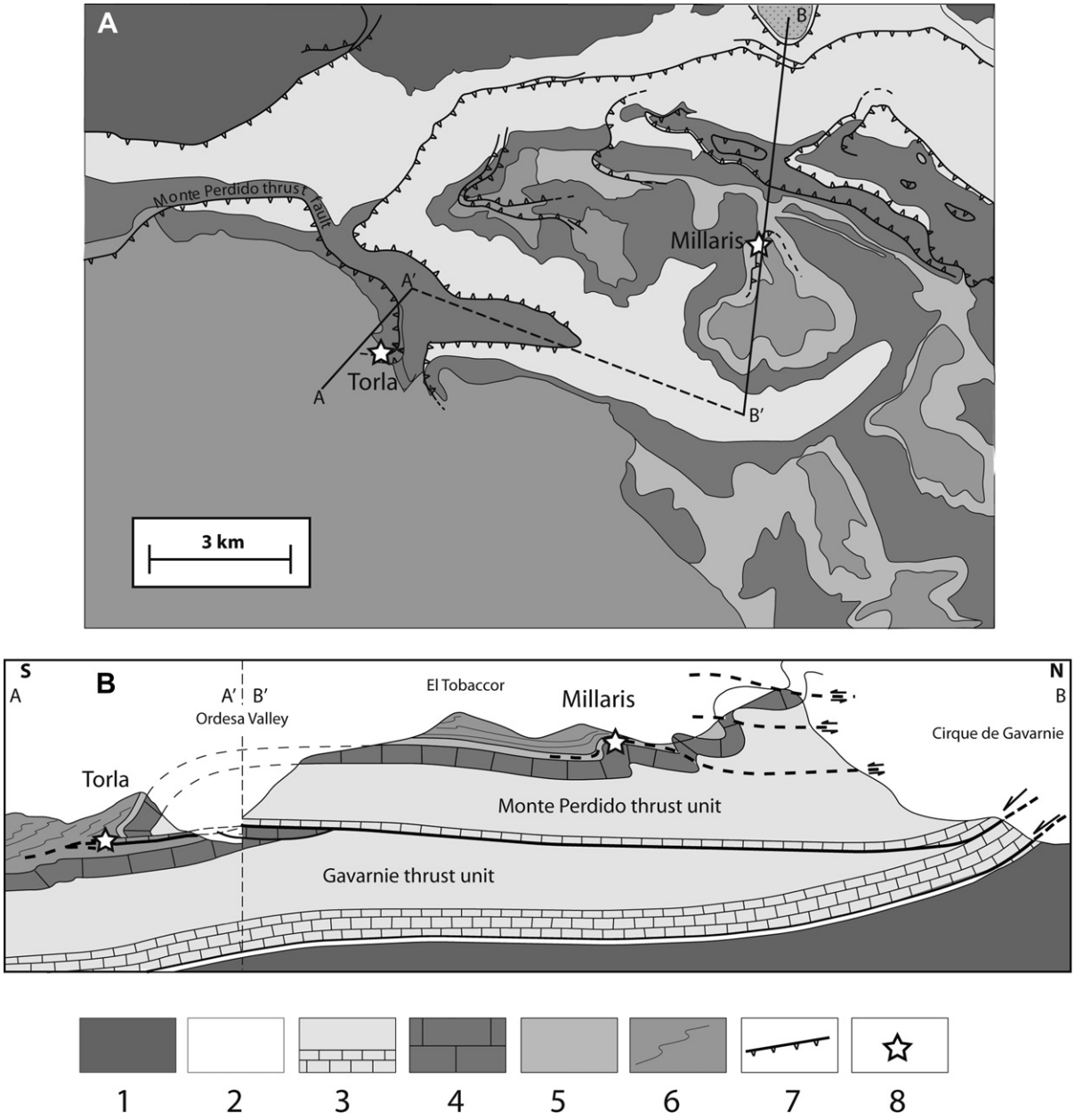

Fig. 2. Geological map (A) and cross-section (B; location: line in A) of the studied area, with the location of the two studied faults. 1: Palaeozoic basement; 2: Triassic; 3: Upper Cretaceous platform limestones (lower part, boxed) and sandy limestones (Marboré sandstone; upper part); 4: Paleocene-lowest Ypresian platform limestones (Alveolina limestone); 5: lower Ypresian Millaris marls; 6: Ypresian Hecho Group turbidites; 7: thrust faults; 8: studied faults. Map simplified from the Bujaruelo and Broto 1:50,000 scale IGME maps; section modified from Séguret (1972).

temperature conditions of vein precipitation, they failed to constrain the pressure and burial conditions of deformation.

The purpose of the present study is to constrain (i) the deformation mechanisms and associated fluid-rock interactions in fault zones and (ii) the burial conditions in which these processes occurred during emplacement of the Monte Perdido thrust unit. Two faults located at different structural positions inside the thrust unit have been studied (Fig. 2): the Monte Perdido thrust fault and the Millaris fault. The former corresponds to the sole thrust of the Monte Perdido thrust unit whereas the latter is a local décollement inside the unit. We have coupled petrographic observations, stable isotope geochemistry and Raman spectrometry on fluid inclusions in order to constrain the deformation processes and the origin of fluids. Microthermometric measurements on fluid inclusions coupled with stable isotope geochemistry results were also used to determine the P-T conditions of syntectonic vein formation. The results demonstrate the multi-stage evolution of the fault zones and constrain the geothermal gradient that affected the Monte Perdido thrust unit during the Eocene deformation.

2. Geological setting

The Pyrenees Mountain Range is a doubly-vergent orogenic wedge formed during convergence between Iberia and Europe from late Cretaceous to early Miocene times, in connection to the northward continental subduction of the Iberian lithosphere (*e.g.* Choukroune et al., 1990; Muñoz, 1992; Teixell, 1998; Beaumont et al., 2000).

From the north to the south, three main structural zones constitute the Pyrenean orogen (Fig. 1A). The North-Pyrenean zone corresponds to a Mesozoic extensional basin system inverted and transported northward by the Pyrenean compression. To the south, the Axial Zone corresponds to the inner part of the south-vergent thrust belt. It comprises Palaeozoic rocks deformed and metamorphosed during the Hercynian orogeny, cross-cut by late-Hercynian granodiorites and locally covered by Permian-lower Triassic sediments. The Alpine structure of the Axial Zone corresponds to imbricated basement thrusts that pass southward to a décollement in the Triassic evaporites (Muchelkalk and Keuper), at the base of the Mesozoic and Tertiary succession forming the South-Pyrenean Zone (Fig. 1B). The latter is affected by a south-vergent thrust-fold system and overthrusts the Ebro foreland basin along the South-Pyrenean Frontal Thrust (SPFT in Fig. 1B). Total shortening across the belt has been estimated from balanced cross-section construction to 165 km in the central Pyrenees (Beaumont et al., 2000) and 80 km in the western Pyrenees (Teixell, 1998), about 70% of which is accumulated in the south-vergent thrust system.

The study area is located at the northern edge of the Jaca thrust-sheet-top basin, which corresponds to the western part of the South-Pyrenean Zone (Fig. 1). Above the Triassic décollement level, the stratigraphy of the Jaca basin comprises Cenomanian to Santonian platform limestones followed by the upper Cretaceous-Paleogene syn-orogenic succession with, from bottom to top, Campanian to earliest Eocene platform carbonates, the Ypresian-Lutetian siliciclastic turbidites of the Hecho Group and Bartonian to Lower Oligocene coastal and continental deposits (*e.g.* Teixell, 1996) (Fig. 1B). At the northern edge of the Jaca basin, the Triassic evaporites are absent and the Cretaceous limestones rest directly on the Palaeozoic basement of the Axial Zone.

The basement structure comprises, from the north to south, the Gavarnie thrust at the southern edge of the Axial Zone and the Bielsa and Guarga thrusts below the northern part of the Jaca basin (*e.g.* Mutti et al., 1988; Teixell, 1996; Jolivet et al., 2007) (Fig. 1B). At the front of the Gavarnie basement thrust unit, the Monte Perdido thrust unit is the uppermost cover thrust unit, detached in the lower part of Upper Cretaceous limestones (Séguret, 1972). Mapping at the western termination of the Axial Zone, where the Cretaceous cover has been preserved (Fig. 1A), shows that the Monte Perdido thrust fault roots in the Lakoura-Eaux-Chaudes basement thrust system, located in the northern part of the Axial Zone (Labaume et al., 1985; Teixell, 1996). To the south, the sole thrust of the Monte Perdido thrust unit cuts up across the Upper Cretaceous-Paleocene carbonates and overlying turbidites. Folds and thrusts located more to the south in Jaca basin are connected to the Gavarnie, Bielsa and Guarga thrusts through the Triassic décollement level.

Thrusting of the Monte-Perdido unit is dated to late Lutetian to earliest Priabonian times (47–37 Ma), during the deposition of the latest Hecho Group turbidites (Teixell, 1996). The northern part of the Monte Perdido thrust unit was then folded and uplifted by the emplacement of the underlying Gavarnie basement thrust unit during the late Eocene–early Oligocene (Séguret, 1972; Teixell, 1996). Basement deformation and related cover structures then propagated southward with activation of the Guarga thrust during the late Oligocene–early Miocene and the out-of-sequence Bielsa thrust during the early Miocene (Jolivet et al., 2007).

A regional pressure solution cleavage related to the emplacement of the Monte Perdido and Gavarnie thrust units is observed in the northern part of the Jaca basin (Séguret, 1972; Labaume et al., 1985; Holl and Anastasio, 1995; Teixell, 1996; Oliva-Urcia et al., 2009). According to Holl and Anastasio (1995), the cleavage front in mudstone is coincident with the ~195 °C paleo-isotherm.

The study area is located at the front of the Monte Perdido thrust unit, on the southern flank of the Monte Perdido massif (Fig. 2). The local stratigraphy comprises, from bottom to top: (1) Upper Cenomanian to Santonian platform limestones, (2) Campanian-Maastrichtian platform sandy limestones (the Marboré sandstone), (3) Paleocene-earliest Ypresian limestones with dolomite and sandstone intercalations (here collectively named the Alveolina limestone), (4) early Ypresian marls (the Millaris marls) and (4) the early Eocene turbidites of the lower part of the Hecho group. Below the Monte Perdido massif, the sole thrust of the Monte Perdido thrust unit is a décollement located in the lower part of the Cenomanian-Santonian limestones (Fig. 2). To the south, the thrust cuts up across the overlying formations with a large hanging wall anticline (Fig. 2B). In the hanging wall, the folding disharmony between the platform carbonates and the turbidites implies accommodation by shearing along the Millaris marls. The area is located below the regional cleavage front (Fig. 1B). Based on illite cristallinity, Holl and Anastasio (1995) determined a maximal temperature of ~217 °C in the lowermost part of the Hecho Group turbidite succession (cf. their 91–27 sample).

Three outcrops of sub-horizontal fault zones related to the Monte Perdido thrusting were studied and sampled. Two outcrops correspond to the Monte Perdido sole thrust (Torla 1 and Torla 2; Torla in Fig. 2). The third one corresponds to a local décollement affecting the Millaris marls inside the Monte Perdido thrust unit (Millaris in Fig. 2).

3. Methods and analytical techniques

Detailed structural analysis was carried out in the field on each of the three selected outcrops. In each one, samples were collected along a vertical transect through the fault zone (Fig. 3). In the fault zone, both mineralised veins and deformed sediments were sampled. Host marls, limestones and turbidite sandstones were also collected up to about 15–30 m away from the fault zone. This distance was determined from macroscopic structural observation in the field so that the most remote samples are not affected by significant deformation related to the major faults but only by background regional deformation.

Petrographic and structural characteristics of 40 samples were studied on standard polished thin sections using the petrographic microscope. Mineral species in samples were identified at the University of Franche-Comté (Besançon, France) with a JEOL JSM5600 scanning electron microscope coupled with a FONDIS energy dispersive analyser (EDS).

Eighty-six microsamples of veins and host rocks were selected from thin section analysis in order to determine the carbon and oxygen stable isotope ratio of calcite. Analyses were performed at the University of Barcelona using the standard technique from Craig and Gordon (1965) and Claypool et al. (1980). The CO_2 was extracted from 60 ± 10 μg of powered carbonate samples which were reacted with 103% phosphoric acid for 2 min at 70 °C for calcites and 15 min at 70 °C for dolomites. The CO_2 was analyzed using an automated Kiel Carbonate Device attached to a Thermal Ionization Mass Spectrometer Thermo Electron (Finnigan) MAT-252. The results are precise to ±0.02‰ for $\delta^{13}C$ and ±0.04‰ for $\delta^{18}O$. Results are reported in permil (‰) values relative to the Vienna PDB standard.

Quartz grains were separated from one vein (see below) by crushing and hand-picking. The oxygen isotope composition (^{16}O, ^{18}O) of the samples was measured at the University of Lausanne, using a method similar to that described by Sharp (1990) and Rumble and Hoering (1994), and described in more detail in Kasemann et al. (2001). Between 0.5 and 2 mg of sample was loaded onto a small Pt-sample holder and pumped out to a vacuum

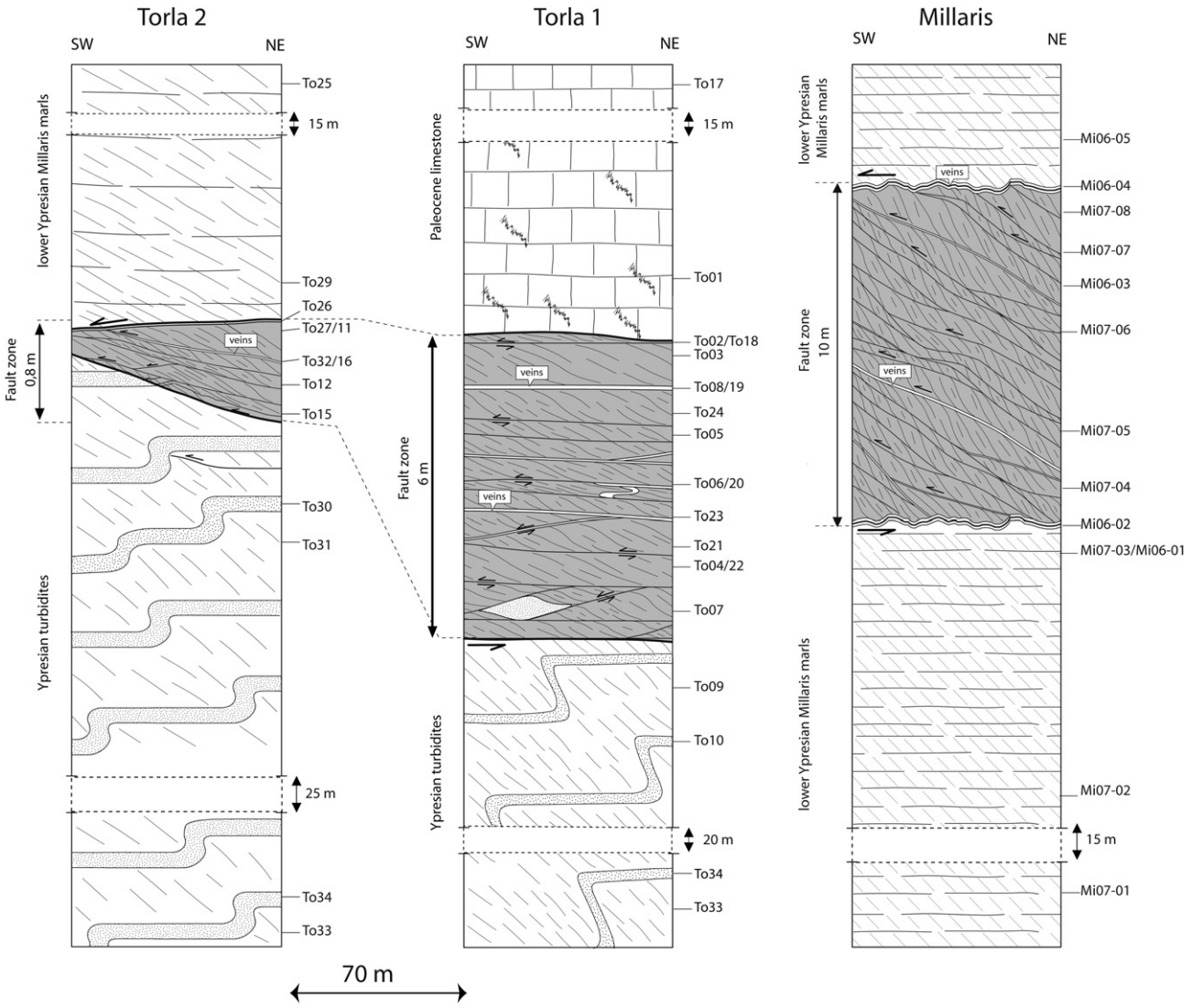

Fig. 3. Schematic diagrams of the structural organization of the three studied fault zone outcrops. The sample locations are labelled as ToXX for the Torla samples and MiXX for the Millaris samples. Samples To33-1 and 34-1 are shown on both Torla outcrops because they originate from an intermediate location between the two outcrops.

of about 10^{-6} mbar. After prefluorination of the sample chamber overnight, the samples were heated with a CO_2-laser in 50 mbars of pure F_2. Excess F_2 was separated from the O_2 produced by conversion to Cl_2 using KCl held at 150 °C. The extracted O_2 was collected on a molecular sieve (13X) and subsequently expanded into the inlet of a Finnigan MAT 253 isotope ratio mass spectrometer. Oxygen isotope compositions are given in the standard δ-notation, expressed relative to VSMOW in permil (‰). Replicate oxygen isotope analyses of the standard used (NBS-28 quartz; or LS-1 Qtz) have an average precision of ±0.1‰ for $\delta^{18}O$. The accuracy of $\delta^{18}O$ values is better than 0.2‰ compared to accepted $\delta^{18}O$ values for NBS-28 of 9.64‰.

Fluid inclusions were analyzed in doubly polished wafers. Considering the relatively small grain size, sections were about 50 μm thick and glued on glass plates using the Geoptic resin (manufactured by Brot Technologies), which can resist freezing and moderate heating (up to 200 °C). They were studied at the Géosystèmes Laboratory (University of Lille 1) by microthermometry using a FLUID INC (USGS-type) heating and freezing stage. The calibration of the microthermometric stage was made using synthetic fluid inclusions (SYNFLINC; Sterner and Bodnar, 1984) including, (1) pure water (ice melting temperature = 0.0 °C; critical homogenization temperature = 374.1 °C), (2) H_2O–CO_2 inclusions (CO_2 melting temperature = −56.6 °C; hydrate melting temperature = +10.0 °C) and (3) H_2O–NaCl inclusions (eutectic temperature = −21.2 °C). Accuracy is ±0.1 °C at temperature between −56.6 and +25 °C and up to about ±1 °C at +400 °C.

As the majority of the observed inclusions contain two-phases (aqueous liquid + gas bubble), two temperatures were measured: (1) homogenization temperature (Th) which indicates the minimum inclusion formation temperature and (2) ice melting temperature (Tm) which is a function of the salt content of the aqueous phase. Inclusions were studied respecting the concept of Fluid Inclusion Assemblage (FIA; Goldstein and Reynolds, 1994; Goldstein, 2003). Each FIA is composed of a few inclusions (generally about 10, but some include only a few ones) taken to be representative of the same trapping event.

Raman microspectrometry was performed at the Géosystèmes Laboratory (University of Lille 1). Raman spectra were recorded with a LabRam HR800 Jobin-Yvon™ microspectrometer equipped with 1800 g/mm gratings and using 532.28 nm (green) laser excitation. Acquisition timespan varied from 20 to 60 s during three

accumulating cycles. Vapour bubbles were systematically investigated in order to evaluate the presence of volatile species (CH_4, CO_2, N_2, H_2S). Analytical problems were encountered due to the small bubble size (often less than 5 μm) and bubble mobility at room temperature. To reduce the latter problem, analyses were carried out at low temperature (about −20 °C) using a microthermometric stage (Linkam THMS600) adapted on the Raman microspectrometer. This configuration significantly reduced the brownian movement of the vapour bubbles.

4. Outcrop descriptions

On each of the three studied outcrops, the fault zone corresponds to a m-thick shear zone characterized by strongly foliated sediments and numerous mineralized veins (Fig. 3). Boundaries of the fault zones are sharp and correspond to Principal Slip Zone (Sibson, 2003). The presence of step-fibre mineralisation and the absence of cataclasite, fault breccias and gouge along the Principal Slip Zone indicate a aseismic slip activity (Gratier and Gamond, 1990). Outside the fault zones, the intensity of deformation is abruptly reduced and mainly corresponds to the regional cleavage and spaced veins and shear zones.

4.1. Torla outcrops

The Torla 1 and 2 outcrops (Fig. 3), located at a distance of ~70 m from each other, correspond to the Monte Perdido sole thrust (Fig. 2). On both outcrops, the footwall comprises Hecho Group turbidites of the Gavarnie thrust unit. In the hanging wall, the thrust cuts up at a low angle from the Alveolina limestone at Torla 1 to the Millaris marls at Torla 2.

The fault zone, ~6 m thick at Torla 1 and 1 m at Torla 2, consists of an interval of intensely deformed clay-bearing rocks bounded by major shear surfaces (Fig. 4A–C). At Torla 1, the presence of decimetric deformed sandstone lenses shows that the fault zone developed in the footwall turbidites, while it developed in the Millaris marls from the hanging wall at Torla 2. Deformation principally resulted in closely-spaced cleavage surfaces associated with cm- to dm-spaced shear surfaces networks in a S-C(C′)-type structure (Fig. 4B–D). The deformed sediment is markedly darker than the protoliths. Calcite-quartz shear veins along the shear planes are abundant (Fig. 4C, E and F) and feature surface striation oriented ~ N030E (Fig. 4E and G). The shear veins are frequently deformed by cm-scale folds with axes oblique to sub-parallel to the transport direction (Fig. 4F). The cleavage orientation, asymmetry of S-C structure and steps along shear vein striation all indicate a displacement towards the S–SW (Fig. 4G).

In the hanging wall, the deformation is marked by stylolites and calcite veins in the Alveolina limestone, and north-dipping cleavage and minor shear zones with m-spacing in the Millaris marls. The footwall turbidites are deformed by cm to m-scale south-vergent folds associated with local shear surfaces and north-dipping axial plane cleavage. The mean orientation of cleavage outside the fault zone around N130°E is similar to that measured in the fault zones (Fig. 4G) and corresponds to that of the regional cleavage (Séguret, 1972; Holl and Anastasio, 1995). All kinematic markers thus indicate a tectonic transport towards the S–SW, sub-perpendicular to the regional structural trend.

4.2. Millaris thrust

This fault zone corresponds to a décollement in the Paleocene Millaris marls (Fig. 2). It may be connected to one of the small thrusts cutting the platform carbonates more to the north, or/and accommodate the disharmony between the long wavelength folding of the underlying platform carbonates and the small wavelength folding in the overlying turbidites.

The Millaris fault zone consists of a ~10 m thick shear zone bounded by major shear surfaces (Fig. 5A). Similarly to the Torla fault, the fault zone is composed of intensely deformed marls darker than the host marls and featuring a well-developed S-C(C′)-type structure (Fig. 5B). Calcite-quartz shear veins are common along the shear surfaces. Centimetre-thick shear veins deformed by late folding and microfaults associated with cleavage development underline the boundaries of the fault zone (Fig. 5C). Deformation intensity sharply decreases outside the fault zone, where the host marl is affected only by the regional cleavage (Fig. 5A). The cleavage displays a similar orientation inside and outside the fault zone, with a mean value of N108°E. The asymmetry of the S-C structure and striation on foliation and shear veins both indicate a displacement towards the S–SW (Fig. 5D), similar to that determined at Torla and also sub-perpendicular to the regional structural trend.

5. Microstructures

5.1. Protoliths

In the protoliths sampled outside fault zones (Millaris marls and Hecho Group turbidites), microscopic and SEM observations show that cleavage consists of discrete surfaces, and the indented morphology of grain boundaries demonstrate that it was developed by pressure solution of calcite grains and, to a lesser extent, quartz grains (Fig. 6A). Clay minerals are often present along the dissolution planes as detrital illite and chlorite stacks of about 10 μm (Fig. 6B).

5.2. Fault zones

The microstructures observed in the fault zones from the three outcrops exhibit pervasive cleavage, five types of mineralized veins, discrete stylolites and folding.

5.2.1. Cleavage

In the fault zones, cleavage is defined by alignement of thin illite particles (<5 μm) (Fig. 6C) and shows a mm-scale S-C(C′) geometry (Fig. 6D) kinematically coherent with that observed at the outcrop scale. Pressure solution is suggested by the indented morphology of quartz grains along cleavage surface and is probably also responsible for the absence of calcite grains relative to the protoliths (Fig. 6C and D).

5.2.2. Calcite-quartz shear veins

These veins (S_V1 veins in the following; Fig. 7) correspond to up to centimetre-thick tabular bodies with metric to decametric lateral extensions and featuring surface striations (see outcrop pictures in Fig. 4C, E, F and 5B, C). The vein cement is composed of blocky calcite (around 95%) and subsidiary quartz (around 5%). The imbrication of calcite and quartz crystals indicates that both minerals precipitated contemporaneously (Fig. 8D; Kirschner et al., 1995; Durney and Ramsay, 1973). The internal structure is identical to that of the shear veins commonly described in sheared fine-grained sediments (Gaviglio, 1986; Labaume et al., 1991; Davison, 1995; Travé et al., 1997; Lee and Wiltschko, 2000; Teixell et al., 2000; Sejourné et al., 2005). It comprises stacked (sub)-millimetre thick sheets parallel to the macroscopic vein, formed by the lateral succession of numerous sub-millimetric rhomb-shaped veinlets separated from each other by thin, locally discontinuous, host-rock bands (Fig. 7B and C). The rhomb-shaped veinlets correspond to incremental pull-apart openings corresponding to a crack-seal mechanism, with the opening sub-parallel to the

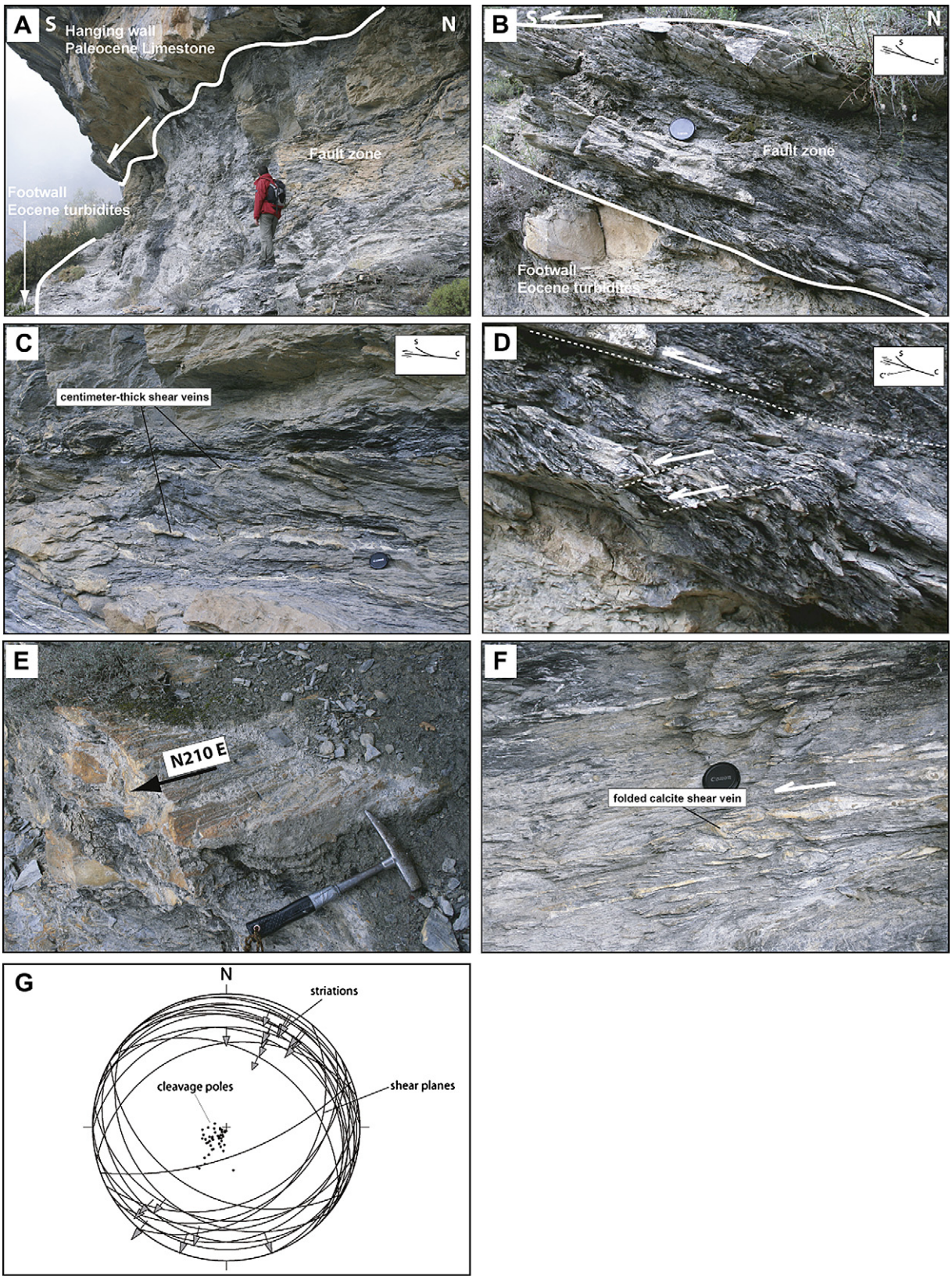

Fig. 4. Field photographs and structural data illustrating the deformation on the Torla fault zone outcrops (*cf.* Fig. 3). A. General view of Torla 1 fault zone. B. General view of Torla 2 fault zone. C. Typical fault zone deformation featuring clay-rich foliated sediment cut by low-dipping shear surfaces, some of the latter being underlined by cm-thick, metre-long veins (Torla 1). D. S-C(C′)-type shear structure (Torla 2, detail of B). E. Striation on a low-dipping calcite shear vein; Sense of movement of the upper block is indicated by the black arrow (Torla 1). F. Folded calcite shear vein (Torla 1). G. Schmidt diagram (lower hemisphere) with plot of cleavage plane poles, shear plane surfaces and striations (arrows indicate the sense of displacement of the upper block); All measured structures indicate thrusting towards the S–SW. Inset diagrams: S, cleavage; C and C′, shear surfaces.

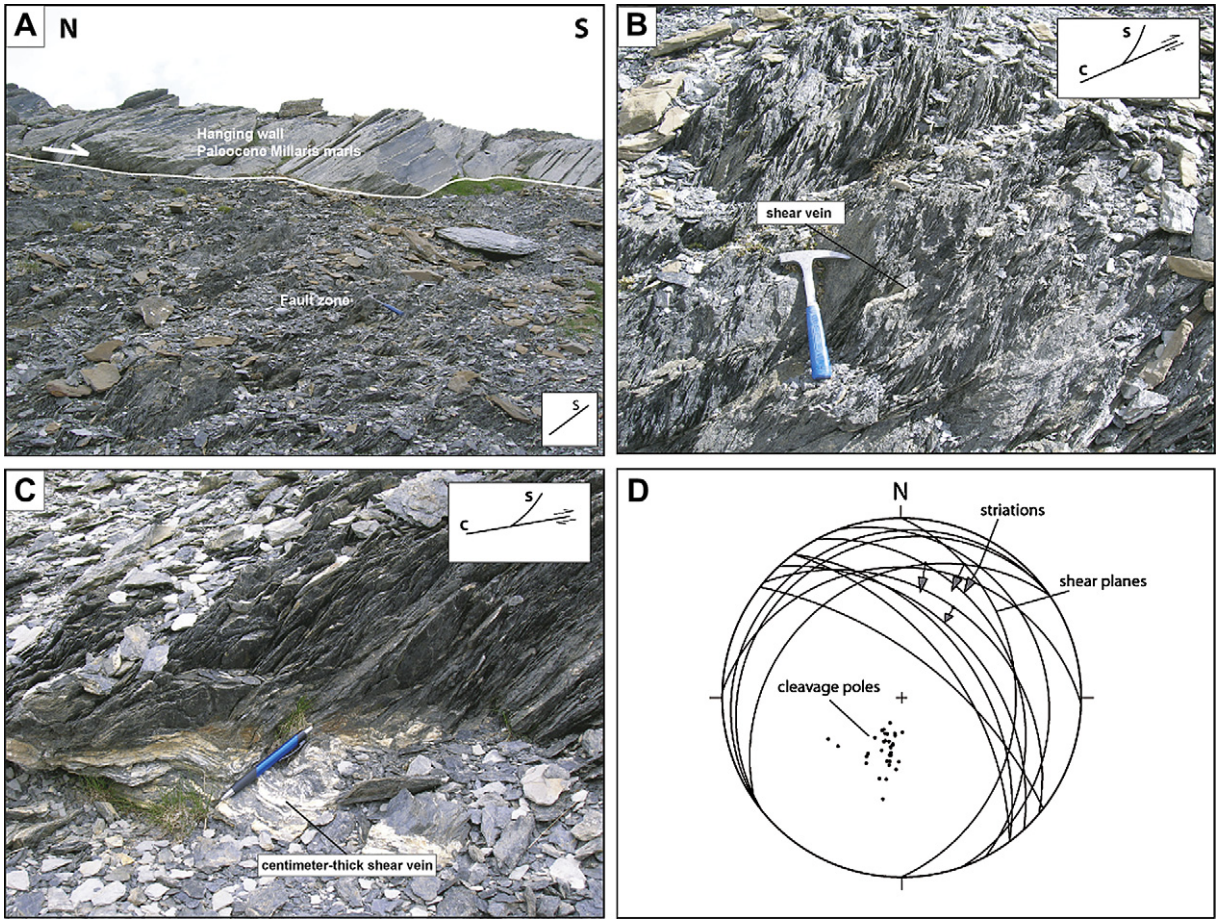

Fig. 5. Field photographs and structural data illustrating the deformation in the Millaris fault zone (*cf.* Fig. 3). A. General view of the fault zone and hanging wall (the footwall is not shown); The fault zone is noticeably darker than the light grey marls of the protolith. B. Detail of deformed sediment inside the fault zone featuring pervasive cleavage and shear surfaces defining a S-C pattern. C. Centimetre-thick calcite shear vein along the lower bounding surface of the fault zone; Note deformation of the vein by folding and microfaults, probably related to cleavage formation in the fault zone. D. Schmidt diagram (lower hemisphere) with plot of cleavage plane poles, shear plane surfaces and striations (arrows indicate the sense of displacement of the upper block); all measured structures indicate thrusting towards the S–SW. Inset diagrams: S, cleavage; C, shear surfaces.

macroscopic vein and obliquity between the shear planes and veinlets giving the sense of shear (*op. cit.*).

5.2.3. Calcite-quartz extension veins

Two types of calcite-quartz extension veins are observed. The first type (henceforth called E_V1) corresponds to thin veins sub-normal to the cleavage and filled with blocky to blocky-elongated calcite and subsidiary quartz crystals (Fig. 7E and F). The C axis of calcite crystals is largely perpendicular to vein walls. The E_V1 veins generally connect to the S_V1 shear veins (Fig. 7E). Fig. 7E shows an example of minor S_V1 veins which cut older E_V1 veins and which are then cut by younger ones (Fig. 7F).

The second type (E_V2) corresponds to extension veins opened across S_V1 shear veins and filled by elongate calcite and quartz crystals, with quartz more abundant than in the E_V1 veins (Fig. 8A–D). Fig. 8B shows a case where a small calcite-chlorite shear vein connects two E_V2 veins and is thus contemporaneous with the latter. Similar to the S_V1 shear veins, the imbrication of calcite and quartz crystals indicates contemporaneous precipitation of both minerals (Fig. 8D).

5.2.4. Chlorite shear veins

The chlorite veins (henceforth called S_V2) occur mainly in the deformed sediment along shear surfaces (C and C′; Fig. 8B, C and E). They also follow boundaries of both S_V1 shear veins and E_V2 extensional veins, or locally cut them (Fig. 8C). The preferred orientation of chlorite particles suggests that they precipitated contemporaneously to the shear movement (Fig. 8E). Chlorite is more abundant along the C′ surface, probably reflecting pull-apart opening along these surfaces, which correspond to extensional surfaces in the S-C-C′ pattern.

5.2.5. Calcite extension veins

The calcite extension veins (henceforth called E_V3) correspond to irregular vein networks filled with blocky (Fig. 9A) to elongated calcite crystals (Fig. 9B). Vein morphology usually follows pre-existing microstructures, such as cleavage, shear surfaces and the other types of veins described above. When present, the calcite fibres are perpendicular to the vein boundaries (Fig. 9B), demonstrating that the E_V3 veins are extensional veins that initially opened with irregular shapes in different directions. Calcite twinning is usually absent or weakly developed and features only thin and rectilinear twinning planes.

5.2.6. Folds and stylolites

Fold and stylolite structures typically affect the S_V1 shear veins, with stylolites sub-parallel to fold axial surfaces (Fig. 8A and B). The folds deform the sediment foliation, but new cleavage can develop along the axial planes of tight folds (Fig. 8B).

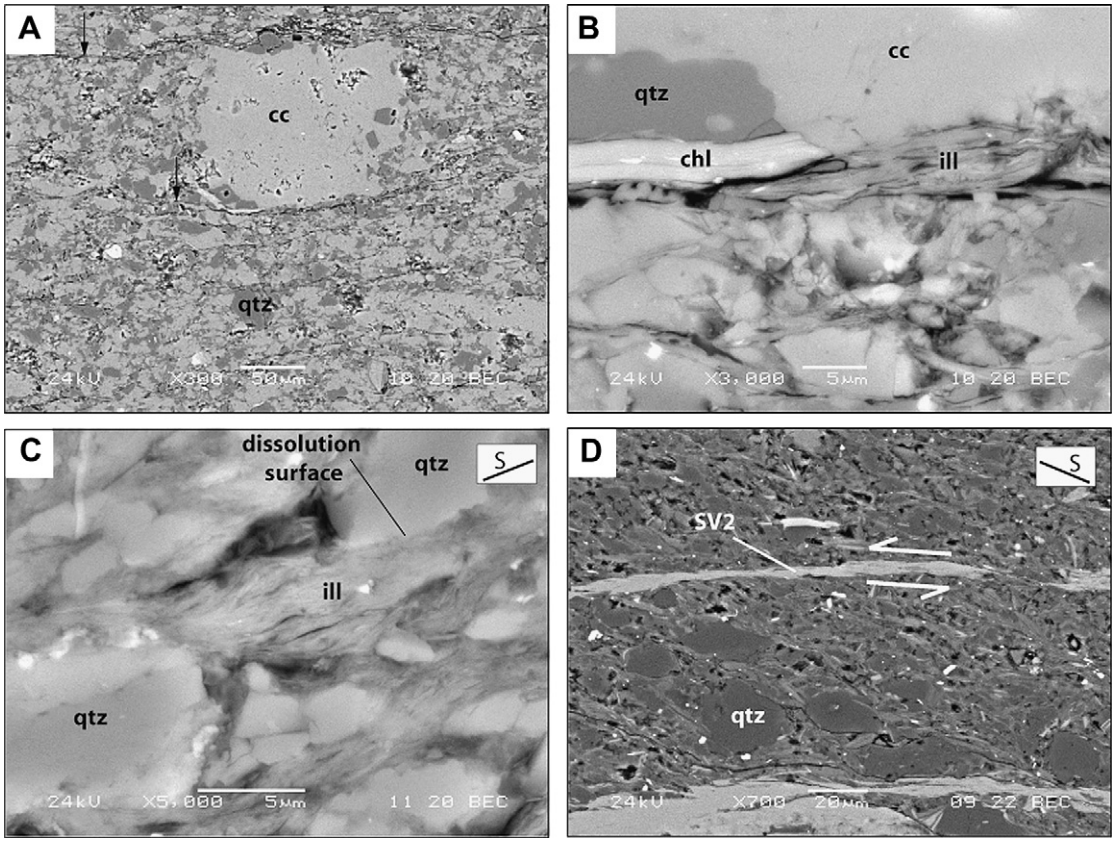

Fig. 6. Backscattered Scanning Electron (BSE) images of cleavage development in protoliths and the fault zone. A. Pressure solution cleavage in the Millaris marls (Millaris outcrop, sample Mi07-01). Cleavage surfaces are indicated by black arrows. B. Detail view showing a concentration of detrital clay particles along a pressure solution surface (Millaris outcrop, sample Mi07-02). C. Preferentially-oriented illite particles determining cleavage in the deformed sediment; Note the lack of calcite and the indentation of detrital quartz grains resulting from pressure solution (Millaris outcrop, sample Mi07-07). D. Relation between chlorite shear vein (*cf.* Fig. 8), cleavage and quartz grains affected by pressure solution (Torla 1 outcrop, sample To21). Cc: calcite; qtz: quartz; chl: chlorite; ill: illite; S: cleavage. Sample labels are located in Fig. 3.

5.2.7. Interpretation of microstructures

Fig. 10 presents a synthesis of all the microstructures observed in a true-scale block diagram. The interpretation below is based on the kinematic and cross-cutting relationships of the different microstructures, the mineralogy of cements in veins and their degree of deformation. We distinguish two stages of shear deformation followed by a late stage of dilatant deformation.

5.2.7.1. Stage I: main shearing deformation. The major shearing deformation is recorded by the association of (i) the pervasive S-C(C′) structure in the clay-rich host sediment where the S surfaces correspond to a closely-spaced pressure solution cleavage, (ii) the S_V1 calcite-quartz shear veins along C and C′ shear surfaces and (iii) the E_V1 calcite-quartz extension veins sub-normal to cleavage. The three types of structures are kinematically coherent with the top-to-the-SSW shear deformation observed at the macroscopic scale, with the shortening and extension directions normal and parallel to cleavage respectively (Fig. 10). The E_V1 veins generally connect to the S_V1 veins, but can locally cut, or be cut by, the S_V1 veins, suggesting that the two types of veins developed during the same global shearing deformation. Pressure solution is interpreted to have increased the clay mineral content of the deformed sediment and to be responsible for its darker colour compared with the protoliths. This suggests that pressure solution of calcite in the sediment may have been the source for calcite precipitation in veins.

5.2.7.2. Stage II: late shearing deformation. All other deformation features post-date those of stage I. The E_V2 calcite-quartz extension veins correspond to boudinage of the S_V1 shear veins. The S_V2 chlorite shear veins are coeval or post-date the E_V2 veins and are interpreted to accommodate the extension related to the E_V2 vein opening in the foliated sediment. Folds and stylolites deform the S_V1 veins and are associated with the transposition of cleavage in the fold axial planes. Top-to-the-SSW shearing deformation (Figs. 8 and 10) is evidenced by: (1) The sense of shear related to the S_V2 veins and to minor calcite-quartz shear veins connected to the E_V2 veins, (2) the extension direction of the E_V2 veins, and (3) the shortening direction that can be deduced from fold axis and stylolites. These relationships suggest that these structures were likely formed during a late stage of deformation, with the typology of structures being mainly controlled by the competence difference between the rigid S_V1 veins and the more deformable host sediment. The SSW-vergence of this late shearing event is coherent with that of the previous main shearing event.

During this late event, the occurrence of newly formed minerals, *i.e.* (i) quartz (in higher abundance in the E_V2 veins than in the S_V1 and E_V1 veins) and (ii) chlorite, could be explained by a change in P-T conditions or by precipitation from a fluid with different chemistry with respect to the main shearing event. These mineralogical differences highlight that the late structures do not result from a local evolution of deformation but correspond to a deformation episode distinct from the main shearing event at the scale of the whole fault zone.

5.2.7.3. Stage III: late dilatancy. The last deformation corresponds to the E_V3 extensional calcite vein systems which opened along previously formed weakness surfaces such as cleavage, shear surfaces and vein walls (Fig. 10). The multidirectional opening thus reflects a late stage of dilatancy of the shearing fabric. The absence

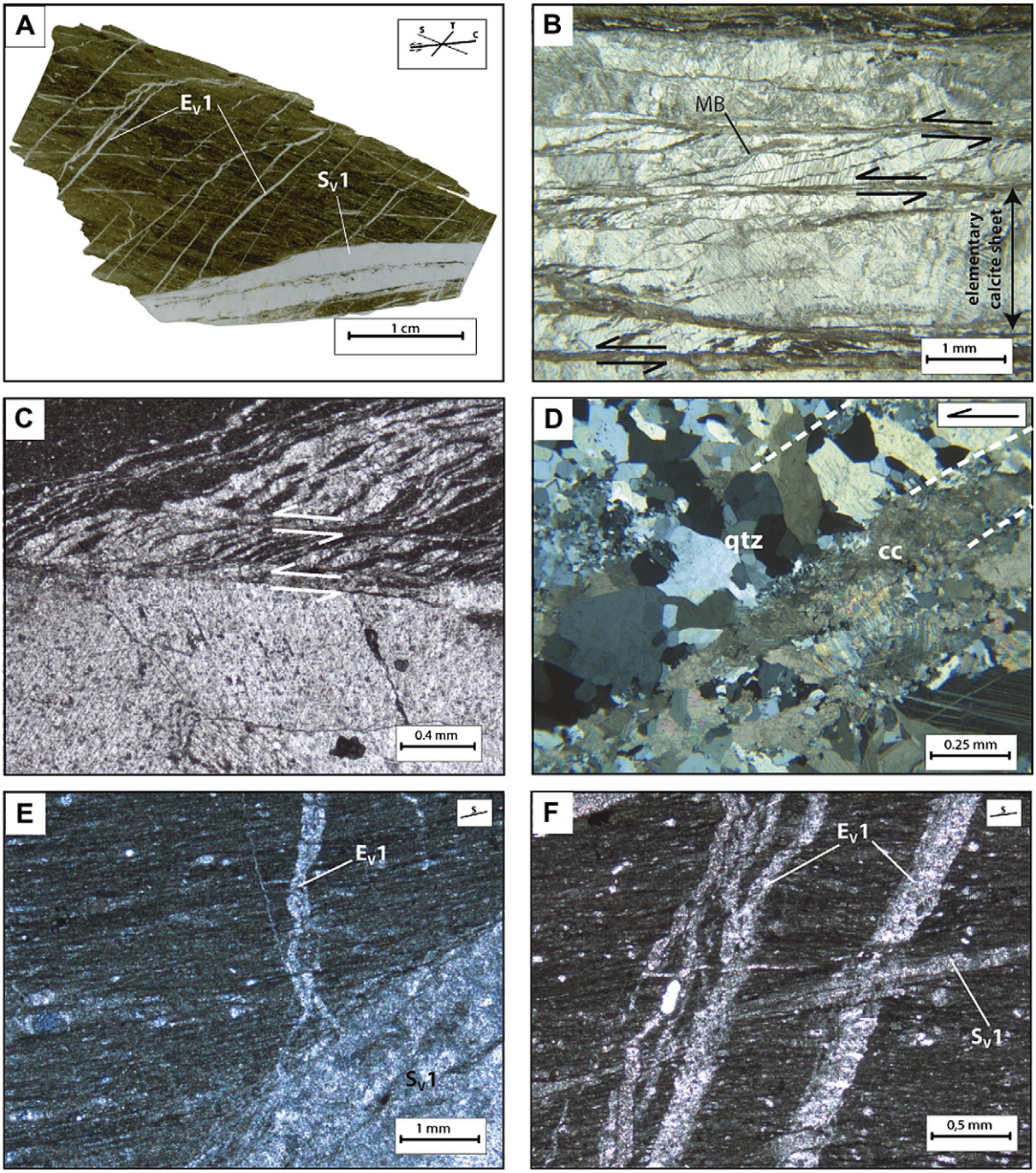

Fig. 7. Thin section (A) and optical microscope (B to F) images of the S_V1 calcite-quartz shear veins and E_V1 calcite-quartz extension veins. A. Thin section illustrating the cm-scale relationships between S_V1 and E_V1 veins and cleavage in the fault zone (Torla 2 outcrop, sample To27). B. General view of the internal structure of a S_V1 vein, with elementary sheets bounded by shear surfaces (arrows); These sheets comprise multiple calcite-filled rhomb-shaped veinlets separated by thin bands of host sediment (MB), corresponding to a crack-seal structure (Torla 2 outcrop, sample To16). C: such as B, with relatively thick bands of host sediment in the upper part and part of a larger rhomb-shaped vein in the lower part (Torla 1 outcrop, sample To03). D: Detail of rhomb-shaped veinlets with both quartz and calcite filling; (Torla 2 outcrop, sample To16). E and F. E_V1 veins cutting cleavage at a high angle; In F, some of the E_V1 veins cut a small S_V1 vein while others are cut by the S_V1 vein (Torla 2 outcrop, sample To27). Sample labels are located in Fig. 3.

or weakness of calcite twinning is coherent with the late formation of the E_V3.

6. Stable isotopes

6.1. Analytical results

Stable isotope analyses have been performed on bulk rocks (protoliths and deformed sediments), calcite cements from S_V1 and E_V1 calcite-quartz veins, and quartz cements from one S_V1 vein. The E_V2 and E_V3 veins were too small to be sampled. Results for calcite are reported in Table 1 and Fig. 11.

6.1.1. Calcite isotopic values

6.1.1.1. Torla outcrops. All calcites from both Torla outcrops yield very similar $\delta^{18}O$ values (Fig. 11A and B). Values (i) from the Millaris marls and Hecho Group turbidites outside fault zones and (ii) from the deformed sediments and S_V1 and E_V1 veins in fault zones, share

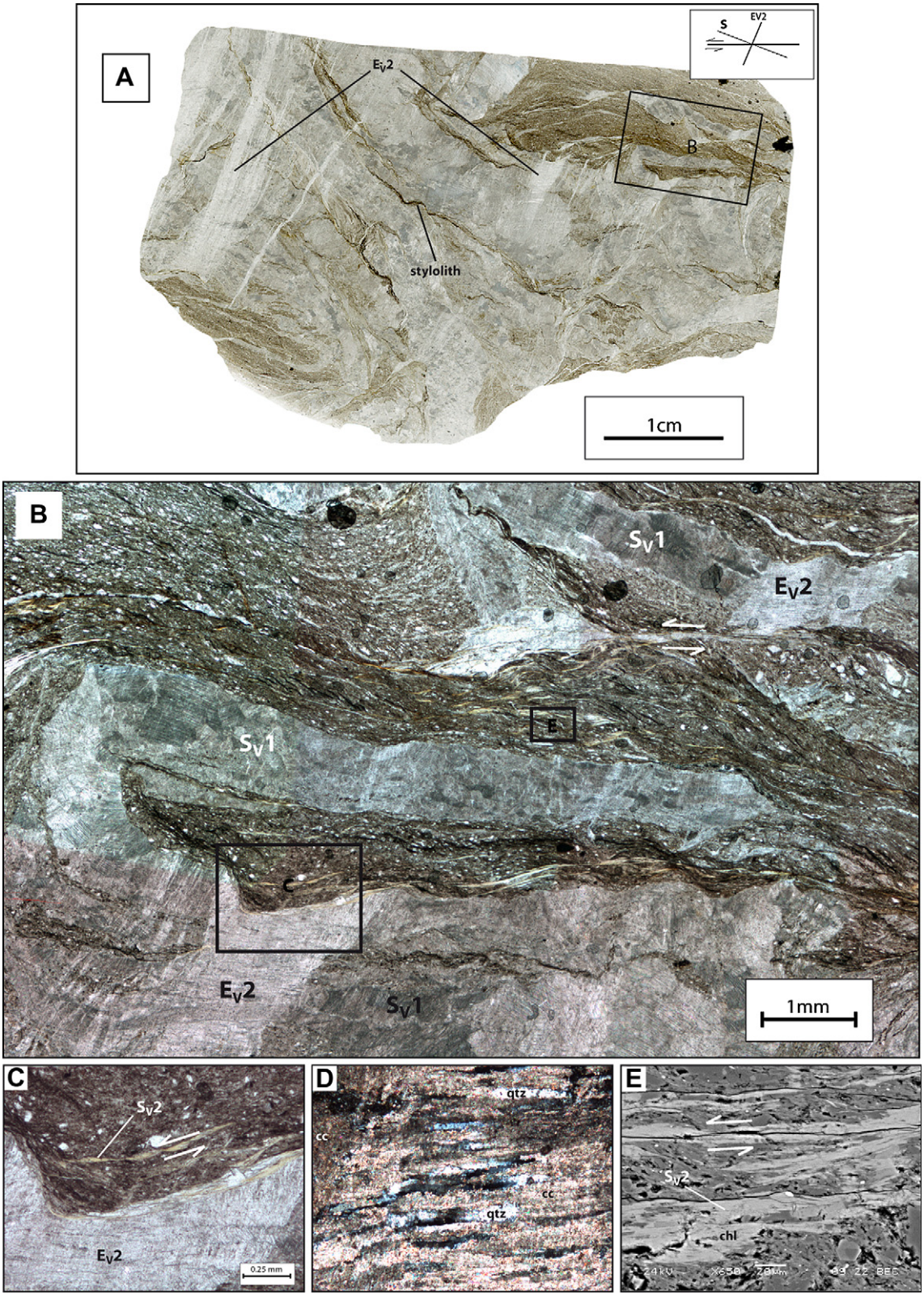

Fig. 8. Thin section (A), optical (B, C and D) and backscattered electron (E) microscope images of the E_V2 calcite-quartz extension veins and S_V2 chlorite shear veins. A. Thin section illustrating folded S_V1 calcite-quartz shear veins cut by E_V2 veins and affected by stylolitization. B. Detail of A showing (i) a S_V1 vein cut by E_V2 veins (boudinage) and (ii) S_V2 veins in the host sediment. C to E. Details from B. (Sample To11, Torla 2 outcrops; sample label is located in Fig. 3).

a narrow range between −8.6 and −7.7‰ VPDB. Values from the hanging wall Alveolina limestone are only slightly less negative, varying between −7.4 and −7.2‰ VPDB.

By contrast, the three protoliths show different $\delta^{13}C$ compositions, varying between −1.2 and 1.3‰ VPDB for the Alveolina limestone, between −1.6 and −1.4‰ VPDB for the Millaris marls

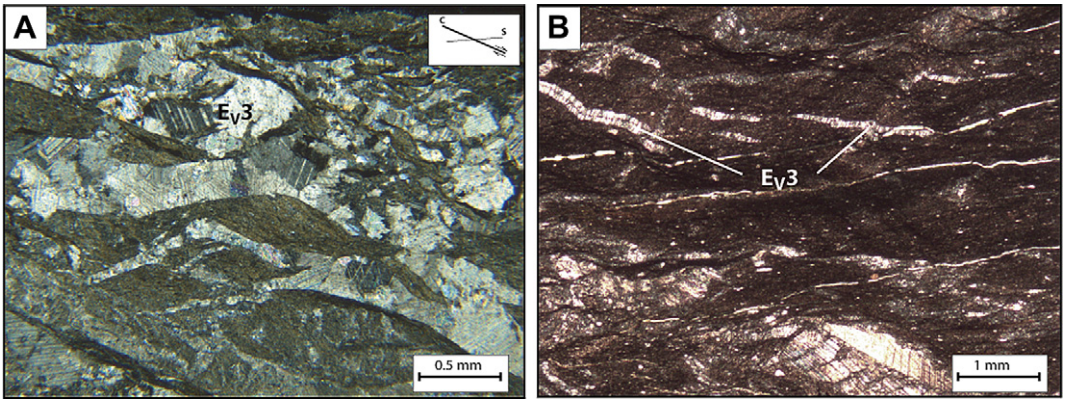

Fig. 9. Optical microscope images of E_V3 calcite extension veins related to dilation of pre-existing structures. A. Blocky calcite in E_V3 veins developed in a S-C structure (Millaris outcrop, sample Mi04). B. Elongated calcite in E_V3 veins developed along cleavage (Millaris outcrop, sample Mi07-08).

and between −6.7 and −4.9‰ VPDB for the Hecho Group turbidites (Fig. 11A and B).

In the fault zones, the $\delta^{13}C$ values of the deformed sediments and S_V1 and E_V1 veins of each outcrop are similar to each other and intermediate between those of the respective hanging wall and footwall protoliths. These values vary between −1.7 and −0.1‰ VPDB at Torla 1 and between −6.1 and −2.6‰ VPDB at Torla 2 (Fig. 11A and B). For both the S_V1 and E_V1 veins, vein-host sediment pairs show isotopic equilibrium between vein cements and their close host sediment (dashed lines in Fig. 11B).

6.1.1.2. Millaris outcrop. Isotopic values of calcites from the protolith (Millaris marls) vary from −7.3 to −6.3‰ VPDB for $\delta^{18}O$ and from −0.7 to −0.2‰ VPDB for $\delta^{13}C$. In the fault zone, isotopic compositions of the deformed sediment present $\delta^{18}O$ values around −7.0‰ VPDB similar to those of the protolith outside the fault zone, and lower $\delta^{13}C$ values varying from −1.4 to −1.0‰ VPDB. The S_V1 and E_V1 veins present $\delta^{18}O$ and $\delta^{13}C$ compositions close to those of the deformed sediment, varying between −7.0 and −6.3‰ VPDB for $\delta^{18}O$ and between −0.5 and −2.5 VPDB for $\delta^{13}C$.

6.1.2. Quartz isotopic values

The $\delta^{18}O$ composition of quartz cement was analysed in one S_V1 shear vein from the Torla 1 outcrop (sample To21; Fig. 3). Two values of 25.9 and 26.1‰ (VSMOW) have been obtained.

6.2. Interpretation of isotopic analyses

The depletion in $\delta^{18}O$ of calcites from the protoliths with respect to Paleocene–Eocene marine carbonates (Fig. 11; Veizer et al., 1999; Prokoph et al., 2008) is interpreted as the reequilibration of the sediment isotopic composition due to fluid-sediment interactions and a temperature increase during burial diagenesis (Longstaffe, 1987 and Longstaffe et al., 2003). The more depleted $\delta^{18}O$ values obtained for the Millaris marls from the Torla outcrops with respect to those from the Millaris outcrop is thus interpreted as the result of a deeper burial depth/higher temperature at Torla. On the latter outcrop, the $\delta^{13}C$ depletion of the Millaris marls and the turbiditic pelites relative to the Alveolina limestone is probably related to the presence of organic matter in the marls and, in higher concentration, in the turbidites.

In both Torla fault zones, calcite from vein is in equilibrium with calcite from the deformed host sediments for both oxygen and carbon isotopes. The $\delta^{18}O$ values are similar to those of the protoliths, while the $\delta^{13}C$ values are variable and intermediary between those of the respective protoliths of each outcrop (Fig. 11A and B). Furthermore, these $\delta^{13}C$ values from fault zones are different in each outcrop, with relatively lower values at Torla 2 than at Torla 1 (Fig. 11A and B). This suggests that fluid in fault zones interacted with local hanging wall and footwall protoliths, with little interaction between both outcrops.

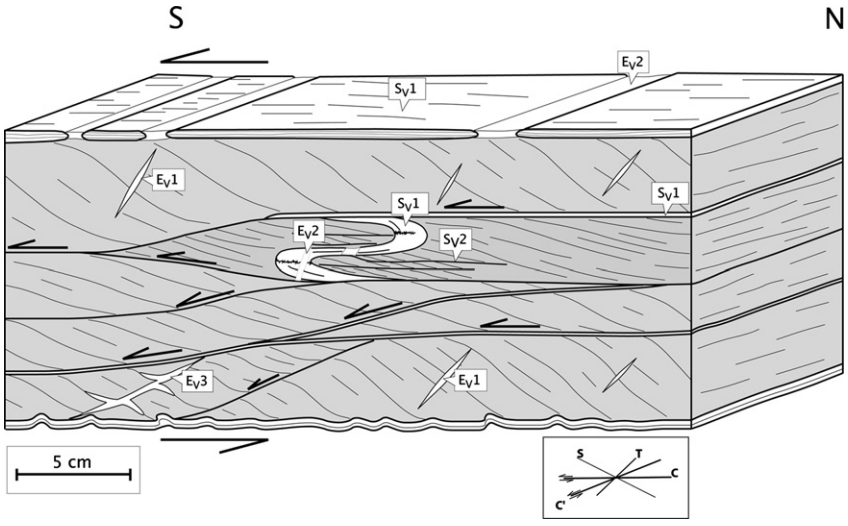

Fig. 10. Block diagram showing the cm-scale geometrical and kinematic relationships between the different types of observed microstructures (*cf.* Figs. 7–9).

Table 1
Oxygen and carbon isotopic data of calcite from Torla and Millaris fault zones outcrops.

Sample	δ^{13}C PDB	δ^{18}O PDB	Description	Location
Millaris Mi01-1	−0.5	−6.8	marl	footwall
Millaris Mi01-2	−0.6	−6.9	marl	footwall
Millaris Mi02b-1	−0.5	−6.6	S_V1	fault zone
Millaris Mi02b-2	−0.5	−6.4	S_V1	fault zone
Millaris Mi03a	−1.0	−7.1	foliated sediment	fault zone
Millaris Mi03b-1	−1.1	−6.9	E_V1	fault zone
Millaris Mi03b-2	−0.9	−6.8	S_V1	fault zone
Millaris Mi04a-1	−1.3	−6.7	E_V1	fault zone
Millaris Mi04a-2	−1.1	−6.3	S_V1	fault zone
Millaris Mi04b	−1.2	−6.3	S_V1	fault zone
Millaris Mi05-1	−0.5	−6.9	marl	hanging wall
Millaris Mi05-2	−0.5	−6.9	marl	hanging wall
Millaris Mi05-3	−0.6	−6.9	marl	hanging wall
Millaris Mi05-4	−0.6	−7.1	marl	hanging wall
Millaris Mi07-01	−0.1	−6.3	marl	footwall
Millaris Mi07-02	−0.4	−6.6	marl	footwall
Millaris Mi07-03	−0.6	−6.8	marl	footwall
Millaris Mi07-06-1	−2.5	−7.0	S_V1	fault zone
Millaris Mi07-06-2	−1.4	−7.0	foliated sediment	fault zone
Millaris Mi07-07	−1.2	−7.0	foliated sediment	fault zone
Torla 1 To01	1.2	−7.4	limestone	hanging wall
Torla 1 To02-1	−0.7	−8.0	S_V1	fault zone
Torla 1 To02-2	−0.1	−7.8	E_V1	fault zone
Torla 1 To02-4	0.1	−8.2	foliated sediment	fault zone
Torla 1 To03-1	−0.7	−8.2	S_V1	fault zone
Torla 1 To03-2	−0.8	−8.1	E_V1	fault zone
Torla 1 To03-3	−0.8	−8.1	S_V1	fault zone
Torla 1 To04-1	−1.5	−8.2	S_V1	fault zone
Torla 1 To04-2	−1.4	−8.1	E_V1	fault zone
Torla 1 To04-3	−1.5	−8.0	E_V1	fault zone
Torla 1 To04-4	−1.3	−8.3	foliated sediment	fault zone
Torla 1 To04-5	−1.0	−8.0	foliated sediment	fault zone
Torla 1 To04-6	−1.5	−7.9	E_V1	fault zone
Torla 1 To04-7	−1.4	−8.1	E_V1	fault zone
Torla 1 To04-8	−1.6	−8.3	E_V1	fault zone
Torla 1 To04-9	−2.6	−8.2	foliated sediment	fault zone
Torla 1 To04-10	−2.6	−8.1	foliated sediment	fault zone
Torla 1 To05-1	−0.9	−8.3	S_V1	fault zone
Torla 1 To05-2	−0.8	−8.2	E_V1	fault zone
Torla 1 To06-1	−1.6	−8.1	S_V1	fault zone
Torla 1 To06-2	−1.7	−8.3	S_V1	fault zone
Torla 1 To07	−1.4	−8.0	S_V1	fault zone
Torla 1 To17-1	1.3	−7.2	limestone	hanging wall
Torla 1 To17-2	1.2	−7.2	limestone	hanging wall
Torla 1 To18-6	−1.0	−8.0	E_V1	fault zone
Torla 1 To18-8	−0.7	−7.1	foliated sediment	fault zone
Torla 1 To21A-1	−1.5	−8.0	E_V1	fault zone
Torla 1 To21A-2	−1.5	−8.0	S_V1	fault zone
Torla 1 To21A-3	−1.4	−8.1	S_V1	fault zone
Torla 1 To22-1	−1.1	−8.0	E_V1	fault zone
Torla 1 To22-2	−1.1	−7.9	E_V1	fault zone
Torla 1 To22-3	−1.2	−8.2	E_V1	fault zone
Torla 1 To22-4	−1.1	−8.2	foliated sediment	fault zone
Torla 1 To33-1	−5.7	−8.5	turbidite pelite	footwall
Torla 1 To34-1	−4.9	−7.6	turbidite sandstone	footwall
Torla 2 To11-1	−5.7	−8.3	S_V1	fault zone
Torla 2 To11-2	−6.1	−8.2	S_V1	fault zone
Torla 2 To11-3	−6.0	−8.5	S_V1	fault zone
Torla 2 To12-3	−5.7	−8.4	foliated sediment	fault zone
Torla 2 To12-1	−5.7	−8.4	foliated sediment	fault zone
Torla 2 To12-2	−5.2	−8.6	S_V1	fault zone
Torla 2 To15-1	−4.1	−8.3	S_V1	fault zone
Torla 2 To15-2	−4.0	−8.0	S_V1	fault zone
Torla 2 To15-3	−2.6	−8.2	S_V1	fault zone
Torla 2 To16-1	−4.6	−8.3	S_V1	fault zone
Torla 2 To16-2	−4.7	−8.4	S_V1	fault zone
Torla 2 To16-3	−4.8	−8.6	S_V1	fault zone
Torla 2 To25-1	−1.4	−8.0	marl	hanging wall
Torla 2 To25-2	−1.6	−8.1	marl	hanging wall
Torla 2 To26-1	−3.9	−8.0	S_V1	fault zone
Torla 2 To26-2	−4.5	−8.6	S_V1	fault zone
Torla 2 To27-1	−3.5	−8.1	S_V1	fault zone
Torla 2 To27-2	−4.3	−8.6	S_V1	fault zone
Torla 2 To27-3	−2.7	−8.2	foliated sediment	fault zone
Torla 2 To28-1	−6.0	−8.4	S_V1	fault zone
Torla 2 To28-2	−5.7	−8.5	S_V1	fault zone
Torla 2 To28-6	−5.9	−8.4	E_V1	fault zone
Torla 2 To31-1	−6.7	−8.2	turbidite pelite	footwall
Torla 2 To32-2	−3.4	−8.1	S_V1	fault zone
Torla 2 To32-3	−4.4	−8.5	S_V1	fault zone
Torla 2 To32-4	−4.3	−8.4	E_V1	fault zone
Torla 2 To32-5	−4.6	−8.5	E_V1	fault zone
Torla 2 To32-6	−4.6	−8.7	S_V1	fault zone
Torla 2 To33-1	−5.7	−8.5	turbidite pelite	footwall
Torla 2 To34-1	−4.9	−7.6	turbidite sandstone	footwall
Torla 2 To35	−1.6	−8.1	marl	hanging wall

Textural and microstructural observations suggest that the calcite and quartz cements analysed in sample To21 (S_V1 shear vein at Torla 1; Fig. 3) precipitated coevally. Then, the temperature of cement precipitation can be constrained assuming that both minerals precipitated from the same fluid. For quartz, Shiro and Sakai (1972) experimentally determined a fractionation factor between quartz and water. The suitability of this experimental fractionation curve was later confirmed by Zheng (1993), who found a similar fractionation curve between quartz and fluid based on empirical bond-type models. Considering the good correlation existing between both approaches, we chose the fractionation factor from Shiro and Sakaï (1972) in order to determine the temperature of S_V1 calcite-quartz shear vein formation. For calcite, Kim and O'Neil (1997) experimentally determined an oxygen fractionation factor between calcite and water. The latter was confirmed by Zheng (1999). Here, we use the fractionation factor between calcite and water provided by Zheng (1999) based on empirical bond-type models. We can thus calculate temperature precipitation from the two following equations:

$$1000\ \ln\alpha_{qtz-H_2O} = 3.55 \times 10^6 T^{-2} - 2.57 \quad (1)$$

(Shiro and Sakai, 1972)

$$1000\ \ln\alpha_{cc-H2O} = 4.010 \times 10^6 T^{-2} - 4.66 \times 10^3 T^{-1} + 1.71 \quad (2)$$

(Zheng, 1999)

Using the δ^{18}O value obtained for calcite and the two values obtained for quartz in sample To21 (Table 1), we obtain two temperatures of 195 and 221 °C. In another hand, using the empirical calcite-quartz thermometry calibrated by Sharp and Kirschner (1994), temperatures of 218 and 232 °C were calculated. These temperature calculation are accurate only if diffusion of oxygen through the calcite and quartz lattice was not fast enough to significantly reset oxygen isotope ratios, a condition likely to have been respected in these low-grade conditions (Kirschner et al., 1995). The calculated temperatures are based on only two quartz oxygen isotopic compositions. Consequently, temperature estimation has to be used with cautions.

7. Fluid inclusions microthermometry

7.1. Analytical results

Fluid inclusions were studied in S_V1 shear veins from the three outcrops and E_V2 extension veins from the Torla outcrops. Due to their small size, the E_V1 and E_V3 extension veins do not contain a significant number of fluid inclusions suitable for a detailed study.

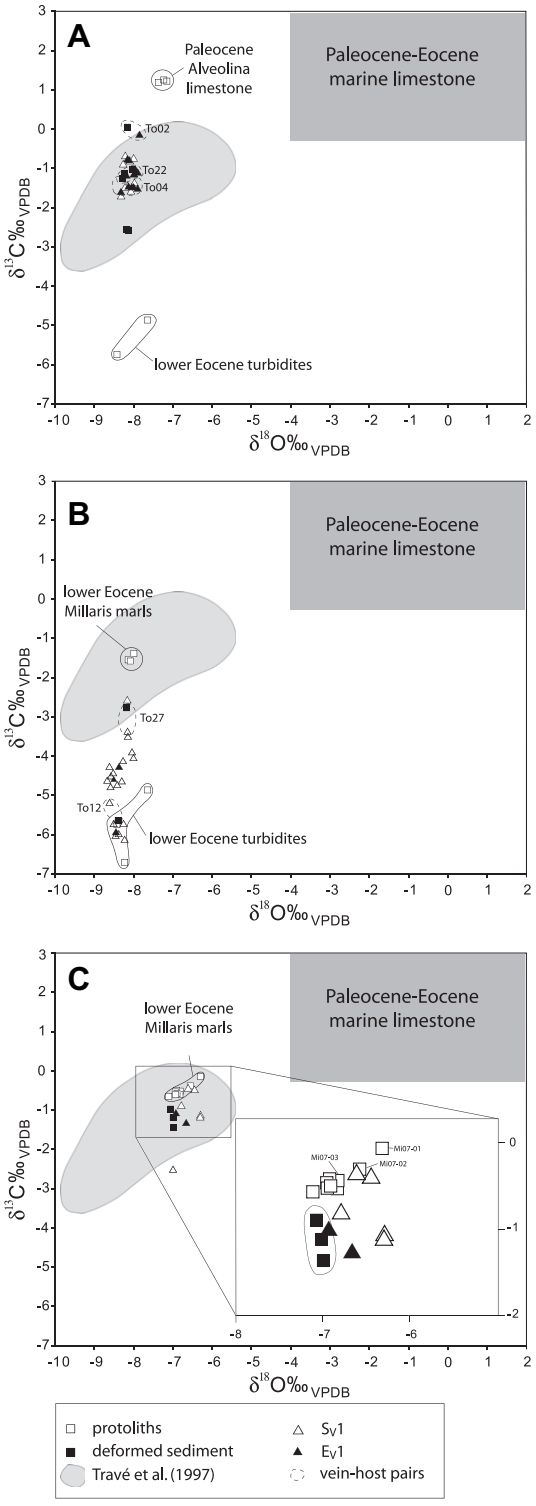

Fig. 11. Cross-plot of the oxygen and carbon isotopic data from the three studied outcrops. A. Torla 1. B. Torla 2. C. Millaris. Sample labels are located in Fig. 3. Analytical results are reported in Table 1. Paleocene and Eocene marine limestone values are from Veizer et al. (1999). Data from Travé et al. (1997) measured on calcite veins and host sediment from the Cotiella thrust faults in the Ypresian turbidites of the Ainsa basin are shown for comparison.

The S_V1 shear veins contain numerous inclusions (3–20 μm), but most of them have a diameter around only 5 μm. Inclusions were observed both in quartz and calcite. They contain two phases at room temperature: An aqueous saline solution and a vapour bubble. Inclusions were classified as primary and secondary on the basis of the Roedder (1984) criteria, complemented by Goldstein (2003). Primary inclusions correspond to fluid entrapped during mineral formation. They are located inside the host mineral. Secondary inclusions are located along fractures and correspond to the fluid that sealed the fracture. The morphologies of inclusions in both calcite and quartz are mostly ovoid to rectangular. The degree of filling (vapour volume relative to bulk volume) is estimated at around 30–40%.

Homogenization temperatures (Th) and melting ice temperatures (Tm) were measured on selected Fluid Inclusion Assemblages (FIA; *cf.* section 4) in calcite and quartz crystals. Ice melting temperatures are less numerous due to the small size of inclusions. Tm measurements range between −3.6 and −0.6 °C. Bulk Th range is between 119.2 °C and 249.5 °C (Fig. 12). Primary inclusions in the S_V1 veins from both the Torla and Millaris outcrops are distributed in a small Th range (165–190 °C) (Fig. 12A). In secondary inclusions, the Th distribution shows a relatively large dispersion (sometimes more than 35 °C) (Fig. 12B). A similar feature is observed for primary inclusions in the E_V2 veins from Torla, but Th are generally higher (range 180–250 °C) (Fig. 12C).

Raman analyses performed on the vapour bubbles indicate the systematic presence of CH_4 in all inclusion types, whatever their chronological position and the host vein type. Narrow peaks were observed between 2915.8 and 2918.3 cm^{-1} in samples To06, To21 and Mi02. No other volatile species were detected.

7.2. Interpretation of fluid inclusions microthermometry

Whereas Raman microanalysis indicates the presence of CH_4 in most inclusions, there is no evidence of clathrate formation upon freezing of the gas phase during microthermometry. In addition, the position of the Raman peaks (2915.8–2918.3 cm^{-1}) is consistent with very low internal pressures at room temperature when extrapolating the data of Fabre and Couty (1986). Therefore, inclusions can be considered as aqueous gas-poor inclusions. In this case, the low-temperature phase behaviour can be used to determine the composition of inclusions (Goldstein and Reynolds, 1994, p. 128). By converting ice melting temperatures into salinities using the equation of Bodnar (1993), the measured range corresponds to a low salinity (between 1.1 and 5.9 wt% eq. NaCl). Salinities of the S_V1 shear vein-hosted inclusions are lower than inclusions in the E_V2 extension veins. This composition corresponds to a sedimentary fluid source with an organic matter component.

In the S_V1 shear veins, the Th values of primary inclusions are distributed in a very restricted range, without significant difference between the Torla and Millaris outcrops (Fig. 12A). Therefore, the mean Th can be considered as representative of the trapped fluid (177 ± 5 °C). Secondary inclusions in the S_V1 veins present a larger temperature range than primary inclusions (161–195 °C) (Fig. 12B). This distribution is interpreted to record the trapping of secondary inclusions at successively higher temperatures.

In the E_V2 extension veins from Torla, the Th values of primary inclusions are significantly higher than in the S_V1 veins (bulk range from 184.3 to 249.5 °C) (Fig. 12C). Th distribution is more scattered and data are considered as "moderately variable" (Goldstein and Reynolds, 1994) in a given FIA. We retain the mode at 195–200 °C as representative of the fluid contemporaneous with E_V2 vein formation.

Isochore calculation should be made taking into account the presence of CH_4. However, our calculation shows that the methane content is probably less than 1000 ppm. In a low salinity fluid (less than 5 wt% NaCl), the pressure shift due to the presence of CH_4 will be about only 22 bar using the model of Duan et al. (1992) relative to the equation state of Zhang and Frantz (1987). Calculated

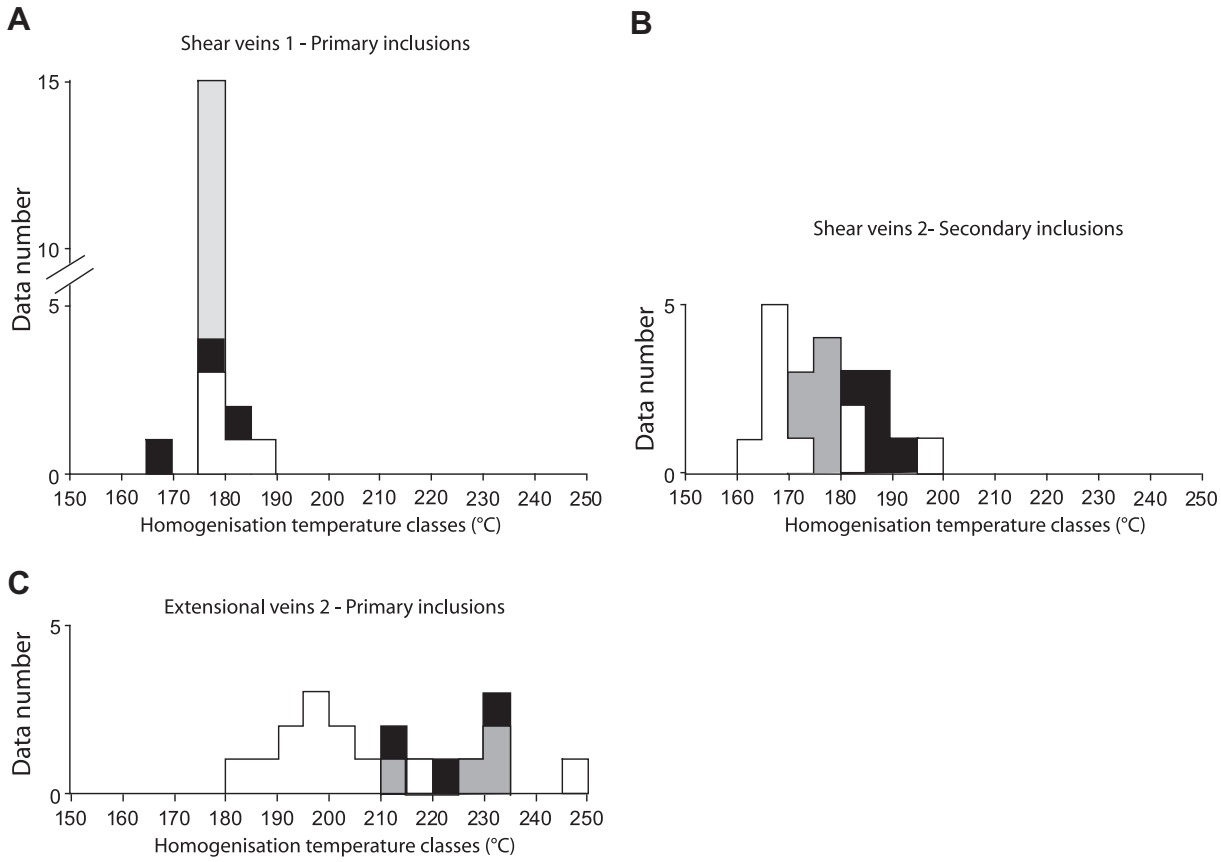

Fig. 12. Frequency plots of measured homogenization temperatures (Th) of fluid inclusions according to the chronology of inclusions and vein types. The different studied Fluid Inclusion Assemblages are differentiated by colour.

isochores of fluid inclusions from S_V1 and E_V2 are represented in Fig. 13. The existence of different isochores for the two types of veins support the interpretation of two distinct shearing episodes presented above (section 5.2.7).

8. Discussion

8.1. Local mass transfer as a major mechanism of aseismic deformation

Pressure solution of calcite and quartz and mineral precipitation in fractures are the major mechanisms in the origin of the structures (cleavage, stylolites and different types of veins) developed during the main and late shearing stages in the studied fault zones. The close spatial association of these structures argues for a fluid-assisted mass transfer process between dissolution surfaces (cleavage and stylolites) and precipitation sites (veins) located at a (sub-) millimetric distance from each other. This thus suggests a closed transfer system, where minerals are dissolved along cleavage and stylolites, and solutes are transported by diffusion to fractures where precipitation occurs (Gratier, 1987; Renard et al., 2000). In the studied samples, mass transfer at the origin of the majority of veins mainly affects calcite, and in a lesser proportion quartz, with the solubility of both minerals depending on P-T conditions. Calcite solubility decreases while quartz solubility increases with increasing temperature (Sharp, 1965; Gratier, 1984). The solubility of both minerals is approximately equal for temperatures around 200 °C (Fyfe et al., 1978). This temperature level corresponds to that determined for the activity of the studied faults, which was thus favourable to the coexistence of calcite and quartz in the studied veins. The transfer process may also have been favoured by the abundance of clay minerals and the small size of quartz and calcite grains exposed to dissolution in the deformed

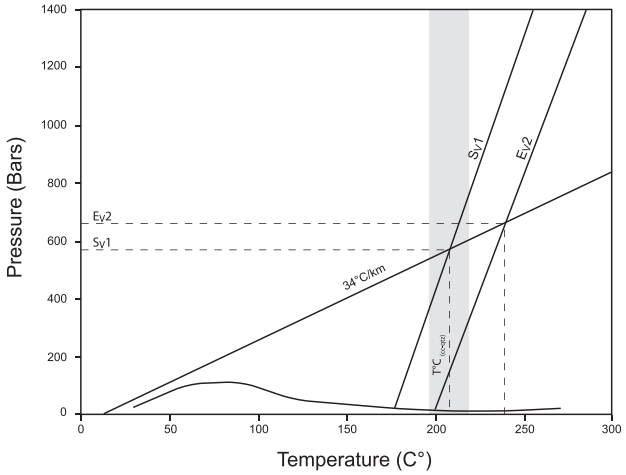

Fig. 13. Temperature–Pressure diagram showing the possible conditions of precipitation of calcite-quartz S_V1 shear veins and E_V2 extension veins as inferred from fluid inclusion microthermometry (*cf.* analytical results in Fig. 12). The bubble point curve (bottom curve) for 1000 ppm methane in a 5 wt% saline solution is drawn using the equation of state of Duan et al. (1992). The isochores for primary inclusions in S_V1 and E_V2 veins are shown. The temperature of precipitation of 208 °C (±13 °C) calculated from stable isotope values of calcite and quartz from a S_V1 vein is plotted (grey column). The hydrostatic geotherm of 34 °C/km is determined from the intersection of the 208 °C temperature with the S_V1 veins isochore. Pressure value for the S_V1 veins and P-T values for the E_V2 veins are deduced from the intersection of the geotherm line with the S_V1 and E_V2 veins isochores, respectively.

sediment, as both features are known to increase the rate of pressure solution (*e.g.* Renard et al., 2000; Bos et al., 2000, Bos and Spiers, 2001; Solum and van der Pluijm, 2009). The association of pressure solutions with a crack-seal mechanism of shear vein formation and the absence of cataclasite and/or gouge argue for slow rate, aseismic deformation (Gratier and Gamond, 1990 and Renard et al., 2000).

8.2. Local fluid origin

In the three studied fault zones, vein calcite cements are in isotopic equilibrium with their host rocks, indicating a very high fluid–rock interaction and the buffering of the fluid by the carbonate fraction of the host rock before calcite precipitation in veins (cf. the vein-host pairs in Fig. 9A and B). In the Torla fault zones, the $\delta^{13}C$ values from deformed sediments and calcite-bearing veins suggest calcite precipitation from a mixing of fluids directly derived from the local hanging wall and footwall lithologies, with different fluid compositions in the two outcrops, located less than 70 m apart. The presence of methane in vapour phases of fluid inclusions from all veins is interpreted to result from thermogenic cracking during burial diagenesis of the organic matter (Goldstein, 2001) found in the Hecho group turbidites and Millaris marls. This assumption is corroborated by the low $\delta^{13}C$ values of vein calcite, which demonstrate the participation of organic-derived carbon in calcite crystallisation. These data suggest a host sediment-derived fluid and support the assumption discussed in the previous section of a local fluid-assisted mass transfer from the host sediment to the mineralised veins in the three studied fault zones. In these conditions, the fluids could have remained essentially static, with solutes transported by diffusion, or flowing over limited distances from the close hanging walls and footwalls towards the fault zones.

The oxygen isotopic compositions of the fluid from which the S_V1 vein calcite and quartz precipitated were determined using the Zheng (1999) equation (sample To12 from Torla). We used the temperature determined by the isotopic fractionation between calcite and quartz (mean value of 210 °C). The calculated $\delta^{18}O$ values of the fluid range from 13.0 to 13.8‰ VSMOW (Fig. 14). These compositions are in agreement with a diagenetic fluid (Longstaffe, 1987), consistent with a local origin of both fluids and solutes from which the vein cements precipitated.

Although isotopic data argue for vein precipitation in a local fluid, deeper fluid sources cannot be neglected. In the Cinca valley, about 10 km NE of the area studied here, Rye and Bradbury (1988) studied the Pineta thrust fault, located in the Upper Cretaceous carbonates of the Monte Perdido thrust unit. Their isotopic data from "en echelon" calcite veins revealed lower $\delta^{18}O$ values in veins compared to their host rocks. A few kilometres northward, McCaig et al. (1995) studied the Gavarnie thrust fault, where they found similar isotopic characteristics. They proposed that the lighter $\delta^{18}O$ composition in veins could be explained by the circulation in the fault zone of a fluid derived from the basement or from the Permian-Triassic red beds rather than a temperature effect as suggested by Rye and Bradbury (1988). In the Ypresian turbidites of the Ainsa basin (~35 km to the SE of the area studied here; Fig. 1), Travé et al. (1997, 1998; 2007) also found lower $\delta^{18}O$ compositions in the thrust-related veins compared to their host sediments. They suggested that this depletion may reflect the circulation of an ascending hot fluid along the fractures. Furthermore, they related the more depleted $\delta^{18}O$ values found in the structurally higher thrust zones to an increasing input of meteoric water when approaching the surface. Due to these variations, the range of $\delta^{18}O$ values is wider in the Ainsa basin fault zones than in the Monte Perdido fault zones studied here (Fig. 11).

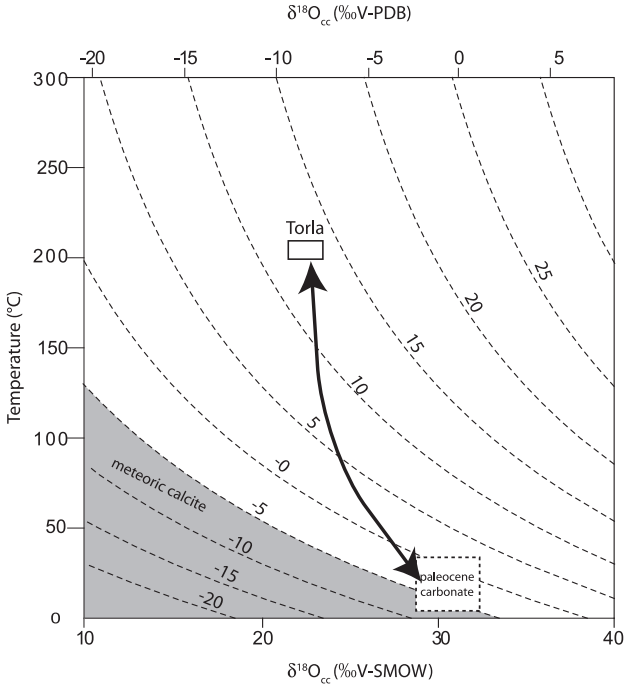

Fig. 14. Isotopic composition of the mineralizing fluid calculated with an oxygen fractionation equation from Zheng (1999). Dashed curve lines correspond to fluid isopleths. Paleocene and Eocene marine limestone values are from Veizer et al. (1999).

In the present study, although the Monte Perdido thrust fault is thought to be linked to the Eaux-Chaudes thrust in the Palaeozoic basement, the $\delta^{18}O$ compositions reveal that fluids in the fault zones were in equilibrium with the deformed host sediments as well as with the adjacent hanging wall and footwall rocks up to a distance of at least ~70 m. This shows that the fault zones were not reached by a potential geochemical front related to the circulation of fluids derived from the basement such as those determined by McCaig et al. (1995) and Rye and Bradbury (1988). These results demonstrate the absence of thermal disequilibrium between the veins and host rocks. In these conditions, it is not possible to quantify a deeper fluid contribution. However, our results indicate that the studied faults did not act as conduits of large fluid fluxes and that circulation, if it existed, remained sufficiently limited in distance or/and volume to allow for the equilibration of fluids with the host rocks.

8.3. P-T conditions of thrusting

The absence of thermal anomaly related to hot fluid flow in fault zones implies that the temperatures derived from stable isotopes and fluid inclusions analyses were primarily determined by the burial depth at the time of deformation.

Microthermometric data on fluid inclusions from vein cements provide two isochores related to the precipitation of the S_V1 shear veins and E_V2 extension veins (Fig. 13). Using the temperature of about 210 °C estimated from the isotopic data, a fluid pressure of ~570 bar is deduced for the precipitation of the S_V1 veins at Torla. With a surface temperature of ~10–15 °C, these P-T conditions correspond to a hydrostatic geothermal gradient of ~34 °C/km. Assuming that this geothermal gradient did not change during the Monte Perdido thrust activity, it can be used to constrain the P-T conditions of the E_V2 extension vein precipitation. Intersection of the E_V2 vein isochore with the 34 °C/km hydrostatic geothermal gradient provides a temperature of ~240 °C with a fluid pressure of ~650 bar.

The assumption of hydrostatic conditions for vein precipitation (see discussion below) implies a burial depth of ~5.7 km for the main shearing episodes (S_V1 shear veins) and ~6.5 km for the late shearing episode (E_V2 extension veins). The former episode corresponds to the emplacement of the Monte Perdido thrust unit during the late Lutetian – early Priabonian. The late shearing episode may correspond to fault reactivation related to the folding of the Monte Perdido thrust unit during the emplacement of the underlying Gavarnie thrust unit (Priabonian – early Oligocene), with deeper burial resulting from aggradation of the thrust-sheet-top basin-fill (Meresse, 2010).

The difference between the $\delta^{18}O$ values from the Millaris and Torla outcrops (Fig. 9) is interpreted to result from the deeper burial depth of the Torla area during burial diagenesis. This assumption is compatible with the currently higher structural positions of the Millaris thrust fault compared to the Torla thrust fault (Fig. 2B).

We note that, based on a thermochronological study, Metcalf et al. (2009) estimated an Oligocene geothermal gradient of 30 °C/km in the central Axial Zone, similar to the modern value (Zeyen and Fernandez, 1994) and close to the value calculated here. On the other hand, in a thermochronological study of the eastern Jaca basin, close to the area studied here, Meresse (2010) showed that apatite fission tracks in the Hecho Group turbidites are only partially reset, suggesting that the temperature at the base of the succession did not exceed 120 °C, or exceeded this value during a too short time for complete reset being reached. Combining this temperature value with the preserved stratigraphic thicknesses, Meresse (2010) assumed a mean geothermal of 25 °C/km and a maximal burial depth of about 5 km for the lowermost turbidites. Our study shows that maximal burial temperature was probably higher, suggesting that the partial reset of apatite fission track may be due to too short a duration at such a temperature.

Contrary to all older structures, the E_V3 dilatant calcite veins are not directly correlated to pressure solution structures. The weak deformation of the vein calcite demonstrates that it was subjected to low stress, and the presence of thin calcite twins can be attributed to a temperature of precipitation and deformation lower than 170 °C (Ferrill et al., 2004). From these characteristics, we infer that the development of the E_V3 veins resulted from the dilatancy of pre-existing weakness surfaces under high fluid pressure during the late exhumation of the Monte Perdido massif.

8.4. Hydrostatic fluid pressure during calcite precipitation

Our determination of the P-T conditions of the Monte Perdido thrust fault activity assumes a hydrostatic geothermal gradient. In low angle extension veins, rupture can occur only under supra-hydrostatic fluid pressure (Hubbert and Rubey, 1959; Sibson, 1985 and Fagereng et al., 2010). However, values close to lithostatic fluid pressure is unrealistic during the Monte Perdido veins precipitation since it would imply a geothermal gradient of up to ~100 °C/km and an overburden sediment thickness of only ~2 km. The overburden Hecho Group thickness during the Monte Perdido emplacement is estimated to ~4500 m (Mutti et al., 1988; Remacha et al., 2003). Considering a sea-water column of ~400–1000 m as suggested by Holl and Anastasio (1995), the fluid pressure of ~570 bar estimated for the main shearing episode is coherent with the hypothesis of a hydrostatic fluid regime. In this context, transient high fluid pressure would have allowed fracture propagation and slip along the low-angle shear veins while precipitation could have recorded a lower, hydrostatic fluid pressure (Wiltschko et al., 2009). This hypothesis is coherent with the model proposed by Robert et al. (1995) where fluid pressure temporally varies in faults with an increasing fluid pressure until lithostatic just before rupture and decrease until hydrostatic during fluid flow following rupture. In such a model, the frequency of fault activity and associated fluid pressure variations are controlled by fault sealing related to pressure solution (Gratier et al., 2009).

9. Conclusions

The macro and microstructural study shows that the main shearing deformation in the Monte Perdido fault zones is characterized by a pervasive pressure solution cleavage associated with calcite-quartz shear and extension veins. A late shearing stage is recorded by veins with a distinct mineralogy, *i.e.* calcite-quartz extension veins with a larger amount of quartz and the occurrence of chlorite shear veins. Dilatant networks of calcite extension veins post-date the shearing deformation.

The oxygen and carbon isotope geochemistry of calcite from veins and host sediment demonstrates that strong fluid–sediment interaction was associated with deformation, with fluid chemistry buffered by host sediments. These chemical characteristics and the close spatial association of pressure solution cleavage with veins suggest a local fluid-assisted mass transfer from the host sediment to the mineralized veins, without necessitating large fluid flow. The dependence of deformation on pressure solution and the crack-seal mechanism of vein opening argue for a slow, aseismic deformation.

The oxygen isotope analyses of cogenetic vein calcite and quartz combined with fluid inclusion microthermometry allow for the determination of the P-T conditions of vein precipitation, *i.e.* ~208 °C/570 bar for the main shearing stage and ~240 °C/650 bar for the late shearing stage. The geological context argues for a hydrostatic geotherm of ~34 °C/km.

The main shearing event is attributed to the emplacement of the Monte Perdido thrust unit during the late Lutetian-early Priabonian under a burial ~5.7 km. The late shearing deformation possibly corresponds to a fault reactivation related to the emplacement of the underlying Gavarnie thrust unit under deeper burial conditions (6.5 km) during the Priabonian-early Oligocene. The late dilatant calcite vein networks record the late exhumation of the massif. This study highlights the potential of combined structural, geochemical and fluid inclusions analyses for determining the P-T conditions of deformation in low-grade sedimentary context.

Acknowledgements

This work was realized within the framework of the 3F "Fault, Fluid, Flow" program funded by INSU-CNRS. Isotopic analyses were realized at the University of Barcelona and University of Lausanne (UNIL). X-ray diffractometry was carried out at the University of Neuchatel.

We thank Nicolas Rouge from the University of Franche-Comté (Besancon) for SEM technical support, Joaquin Perona Moreno from the University of Barcelona for stable isotope analysis, Torsten Vennemann and Benita Putlitz for discussion and analytical support on quartz oxygen isotope analysis and Andrew McCaig and an anonymous reviewer for their constructive reviews improving the manuscript.

References

Barker, S.L.L., Cox, S.F., Eggins, S.M., Gagan, M.K., 2006. Microchemical evidence for episodic growth of antitaxial veins during fracture-controlled fluid flow. Earth and Planetary Science Letters 250, 331–344.

Beaumont, C., Muñoz, J.A., Hamilton, J., Fullsack, P., 2000. Factors controlling the Alpine evolution of the central Pyrenees inferred from a comparison of observations and geodynamical models. Journal of Geophysical Research-Solid Earth 105, 8121–8145.

Bodnar, R.J., 1993. Revised equation and table for determining the freezing point depression of H_2O–NaCl solutions. Geochimica et Cosmochimica Acta 57 (3), 683–684.

Bos, B., Peach, C.J., Spiers, C.J., 2000. Frictional-viscous flow of simulated fault gouge caused by the combined effects of phyllosilicates and pressure solution. Tectonophysics 327 (3–4), 173–194.

Bos, B., Spiers, C.J., 2001. Experimental investigation into the microstructural and mechanical evolution of phyllosilicate-bearing fault rock under conditions favouring pressure solution. Journal of Structural Geology 23 (8), 1187–1202.

Buatier, M.D., Travé, A., Labaume, P., Potdevin, J.L., 1997. Dickite related to fluid-sediment interaction and deformation in Pyrenean thrust fault zones. European Journal of Mineralogy 9 (4), 875–888.

Caja, M.A., Permanyer, A., Marfil, R., Al-Aasm, I.S., Martín-Crespo, T., 2006. Fluid flow record from fracture-fill calcite in the Eocene limestones from the South-Pyrenean Basin (NE Spain) and its relationship to oil shows. Journal of Geochemical Exploration 89 (1–3), 27–32.

Choukroune, P., Roure, F., Pinet, B., Ecors Pyrenees, T., 1990. Main results of the ECORS Pyrenees profile. Tectonophysics 173 (1–4), 411–423.

Claypool, G.E., Holser, W.T., Kaplan, I.R., Sakai, H., Zak, I., 1980. The age curves of sulfur and oxygen isotopes in marine sulfate and their mutual interpretation. Chemical Geology 28, 199–260.

Craig, H., Gordon, L.I., 1965. Deuterium and oxygen-18 variations in the ocean and the marine atmosphere. In: Tongiorgi, E. (Ed.), Proceedings of a Conference on Stable Isotopes in Oceanographic Studies and Paleotemperatures, pp. 9–130.

Davison, I., 1995. Fault slip evolution determined from crack-seal veins in pull-aparts and their implications for general slip models. Journal of Structural Geology 17, 1025–1034.

Duan, Z., Møller, N., Greenberg, J., Weare, J.H., 1992. The prediction of methane solubility in natural waters to high ionic strength from 0 to 250°C and from 0 to 1600 bar. Geochimica et Cosmochimica Acta 56 (4), 1451–1460.

Durney, D.W., Ramsay, J.G., 1973. Incremental strains measured by syntectonic crystal growths. In: De Jong, K.A., Scholten, R. (Eds.), Gravity and Tectonics. John Wiley, New York, pp. 67–96.

Fabre, D., Couty, R., 1986. Etude, par microspectrométrie Raman, du méthane comprimé jusqu'à 3 kbar. Application à la mesure de pression dans les inclusions fluides contenues dans les minéraux. In: Compte-Rendu de l'Académie des Sciences de Paris, 303, pp. 1305–1308.

Fagereng, A., Remitti, F., Sibson, R.H., 2010. Shear veins observed within anisotropic fabric at high angles to the maximum compressive stress. Nature Geoscience 3, 482–485.

Ferrill, D.A., Morris, A.P., Evans, M.A., Burkhard, M., Groshong, R.H., Onasch, C.M., 2004. Calcite twin morphology: a low-tempeature deformation geothermometer. Journal of Structural Geology 26 (8), 1521–1529.

Ferket, H., Roure, F., Swennen, R., Ortuño, S., 2000. Fluid migration placed into the deformation history of fold-and-thrust belts: an example from the Veracruz basin (Mexico). Journal of Geochemical Exploration 69–70, 275–279.

Ferket, H., Swennen, R., Ortuño, S., Roure, F., 2003. Reconstruction of the fluid flow history during Laramide forelandfold and thrust belt development in eastern Mexico: cathodoluminescence and $\delta^{18}O$–$\delta^{13}C$ isotope trends of calcite-cemented fractures. Journal of Geochemical Exploration 78–79, 163–167.

Ferket, H., Swennen, R., Ortuño Arzate, S., Roure, F., 2006. Fluid flow evolution in petroleum reservoirs with a complex diagenetic history: an example from Veracruz, Mexico. Journal of Geochemical Exploration 89 (1–3), 108–111.

Fisher, Q.J., Knipe, R.J., 2001. The permeability of faults within siliciclastic petroleum reservoirs of the North Sea and Norwegian Continental Shelf. Marine and Petroleum Geology 18 (10), 106–1081.

Fyfe, W.S., Price, N.J., Thompson, A.B., 1978. Fluids in the Earth's Crust. Elsevier, Amsterdam.

Gaviglio, P., 1986. Crack-seal mechanism in a limestone: a factor of deformation in strike-slip faulting. Tectonophysics 131, 247–255.

Goldstein, R.H., Reynolds, T.J., 1994. Systematics of fluid inclusions in diagenetic minerals. SEPM short course. Society for Sedimentary Geology 31, 199.

Goldstein, R.H., 2001. Fluid inclusions in sedimentary and diagenetic systems. Lithos 55, 159–193.

Goldstein, R.H., 2003. Petrographic Analysis of Fluid Inclusions. Mineralogical Association of Canada, Vancouver (Canada), pp. 9–53.

Grant, N.T., 1990. Episodic discrete and distributed deformation: consequences and controls in a thrust culmination from the central Pyrenees. Journal of Structural Geology 12 (7), 835–850.

Gratier, J.P., 1984. La deformation des roches par dissolution-cristallisation: aspects naturels et expérimentaux de ce fluage avec transfert de matière dans la croûte supérieure. Thèse d'état. Université de Grenoble.

Gratier, J.P., 1987. Pressure Solution-deposition Creep and Associated Tectonic Differentiation in Sedimentary Rocks. In: Geological Society Special Publication, 29, pp. 25–38.

Gratier, J.P., Gamond, J.F., 1990. Transition between seismic and aseismic deformation in the upper crust. In: Knipe, R.J., Rutter, E.H. (Eds.), Deformation Mechanisms, Rheology and Tectonics. Geological Society Special Publication, vol. 54, pp. 461–473.

Gratier, J.P., Guiguet, R., Renard, F., Jenatton, L., 2009. A pressure solution creep law for quartz from indentation experiments. Journal of Geophysical Research, 114.

Henderson, I.H.C., McCaig, A.M., 1996. Fluid pressure and salinity variations in shear zone-related veins, central Pyrenees, France: implications for the fault-valve model. Tectonophysics 262 (1–4), 321–348.

Holl, J.E., Anastasio, D.J., 1995. Cleavage development within a foreland fold and thrust belt, southern Pyrenees, Spain. Journal of Structural Geology 17, 357–369.

Hubbert, M.K., Rubey, W.W., 1959. Role of fluid pressure in mechanics of overthrust faulting. Geological Society of America Bulletin 70, 115–160.

Jolivet, M., Labaume, P., Monié, P., Brunel, M., Arnaud, N., Campani, M., 2007. Thermochronology constraints for the propagation sequence of the south Pyrenean basement thrust system (France-Spain). Tectonics 26, TC5007.

Kasemann, S., Meixner, A., Rocholl, A., Vennemann, T., Schmitt, A., Wiedenbeck, M., 2001. Boron and oxygen isotope composition of certified reference materials NIST SRM 610/612, and reference materials JB-2G and JR-2G. Geostandards Newsletter V 25, 405–416.

Kenis, I., Muchez, P., Sintubin, M., Mansy, J.L., Lacquement, F., 2000. The use of a combined structural, stable isotope and fluid inclusion study to constrain the kinematic history at the northern Variscan front zone (Bettrechies, northern France). Journal of Structural Geology 22 (5), 589–602.

Kim, S.T., O'Neil, J.R., 1997. Equilibrium and nonequilibrium oxygen isotope effects in synthetic carbonates. Geochimica et Cosmochimica Acta 61, 3461–3475.

Kirschner, D.L., Sharp, Z.D., Masson, H., 1995. Oxygen isotope thermometry of quartz-calcite veins: unraveling the thermal-tectonic history of the subgreenschist facies Morcles nappe (Swiss Alps). Geological Society of America Bulletin 107 (10), 1145–1156.

Labaume, P., Seguret, M., Seyve, C., 1985. Evolution of a turbiditic foreland basin and analogy with an accretionary prism: example of the Eocene South-Pyrenean Basin. Tectonics 4, 661–685.

Labaume, P., Berty, C., Laurent, P., 1991. Syn-diagenetic evolution of shear structures in superficial nappes: an example from the Northern Apennines (NW Italy). Journal of Structural Geology 13 (4), 385–398.

Lacombe, O., Malandain, J., Vilasi, N., Amrouch, K., Roure, F., 2009. From paleostresses to paleoburial in fold-thrust belts: preliminary results from calcite twin analysis in the Outer Albanides. Tectonophysics 475 (1), 128–141.

Lee, Y.-J., Wiltschko, D.V., 2000. Fault controlled sequential vein dilation: competition between slip and precipitation rates in the Austin Chalk, Texas. Journal of Structural Geology 22, 1247–1260.

Longstaffe, F.J., 1987. Stable Isotope Studies of Diagenetic Studies, vol. 13. Mineralogical Association of Canada, Short Course pp. 225–262.

Longstaffe, F.J., Calvo, R., Ayalon, A., Donaldson, S., 2003. Stable isotope evidence for multiple fluid regimes during carbonate cementation of the Upper Tertiary Hazeva Formation, Dead Sea Graben, southern Israel. Journal of Geochemical Exploration 80 (2–3), 151–170.

Marquer, D., Burkhard, M., 1992. Fluid circulation, progressive deformation and mass-transfer processes in the upper crust: the example of basement-cover relationships in the External Crystalline Massifs, Switzerland. Journal of Structural Geology 14, 1047–1057.

McCaig, A.M., Wayne, D.M., Marshall, J.D., Banks, D., Henderson, I., 1995. Isotopic and fluid inclusion studies of fluid movement along the Gavarnie Thrust, central Pyrenees; reaction fronts in carbonate mylonites. American Journal of Science 295 (3), 309–343.

McCaig, A.M., Tritlla, J., Banks, D.A., 2000. Fluid mixing and recycling during Pyrenean thrusting: evidence from fluid inclusion halogen ratios. Geochimica et Cosmochimica Acta 64, 3395–3412.

Meresse, F., 2010. Dynamique d'un prisme orogénique intracontinental: évolution thermochronologique (traces de fission sur apatite) et tectonique de la Zone Axiale et des piedmonts des Pyrénées centro-occidentales. Thèse de doctorat, Université Montpellier 2.

Metcalf, J.R., Fitzgerald, P.G., Baldwin, S.L., Muñoz, J.-A., 2009. Thermochronology of a convergent orogen: constraints on the timing of thrust faulting and subsequent exhumation of the Maladeta Pluton in the Central Pyrenean Axial Zone. Earth and Planetary Science Letters 287 (3–4), 488–503.

Muñoz, J.A., 1992. Evolution of a continental collision belt: ECORS-Pyrenees crustal balanced cross-section. In: MCCLAY, K.R. (Ed.), Thrust Tectonics. Chapman and Hall, London, pp. 235–246.

Mutti, E., Séguret, M., Sgavetti, M., 1988. Sedimentation and deformation in the Tertiary sequences of the southern Pyrenees. In: Field Trip 7 guidebook, AAPG Mediterranean Basins Conference, Nice, France Special Publication of the Institute of Geology of the University of Parma, Parma, Italy.

Oliva-Urcia, B., Larrasoaña, J.C., Pueyo, E.L., Gil, A., Mata, P., Parés, J.M., Schleicher, A.M., Pueyo, O., 2009. Disentangling magnetic subfabrics and their link to deformation processes in cleaved sedimentary rocks from the Internal Sierras (west central Pyrenees, Spain). Journal of Structural Geology 31 (2), 163–176.

Prokoph, A., Shields, G.A., Veizer, J., 2008. Compilation and time-series analysis of a marine carbonate $\delta^{18}O$, $\delta^{13}C$, 87Sr/86Sr and $\delta^{34}S$ database through Earth history. Earth-Science Reviews 87 (3–4), 113–133.

Remacha, E., Gual, G., Bolaño, F., Arcuri, M., Oms, O., Climent, F., Crumeyrolle, P., Fernández, L.P., Vicente, J.C., Suárez, J., 2003. Sand-rich turbidite systems of the Hecho Group from slope to the basin plain: facies, stacking patterns, controlling factors and diagnostic features. In: American Association of Petroleum Geologists, International Conference and Exhibition, Barcelona, Spain, September 21–24 Geological Field Trip No. 12, South-Central Pyrenees.

Renard, F., Gratier, J.-P., Jamtveit, B., 2000. Kinetics of crack-sealing, intergranular pressure solution, and compaction around active faults. Journal of Structural Geology 22 (10), 1395–1407.

Robert, F., Boullier, A.M., Firdaous, K., 1995. Gold-quartz veins in metamorphic terranes and their bearing on the role of fluids in faulting. Journal of Geophysical Research 100 (12), 861–912.

Roedder, E., 1984. Fluid Inclusions. In: Reviews in Mineralogy, vol. 12. Mineralogical Society of America.

Roure, F., Alzaga-Ruiz, H., Callot, J.P., Ferket, H., Granjeon, D., Gonzalez-Mercado, G.E., Guihaumou, N., Lopez, M., Mougin, P., Ortuno-Arzate, S., Séranne, M., 2009. Long lasting interactions between tectonic loading, unroofing, post-rift thermal subsidence and sedimentary transfers along the western margin of the Gulf of Mexico: some insights from integrated quantitative studies. Tectonophysics 475 (1), 169–189.

Rumble, D., Hoering, T.C., 1994. Analysis for oxygen and sulfur isotope ratios in oxide and sulfide minerals by spot heating with a carbon dioxide laser in a fluorine atmosphere. Accounts of Chemical Research 27 (8), 237.

Rye, D., Bradbury, H.J., 1988. Fluid flow in the crust: an example from a Pyrenean thrust ramp. American Journal of Science 288, 197–235.

Séguret, M., 1972. Etude tectonique des nappes de séries décollées de la partie centrale du versant sud des Pyrénées. Caractère synsédimentaire, rôle de la compression et de la gravité. Thèse Doct. Publ. USTELA, Série Géologique, Montpellier, 155 pp.

Séjourné, S., Malo, M., Savard, M.M., Kirkwood, D., 2005. Multiple origin and regional significance of bedding parallel veins in a fold and thrust belt: the example of a carbonate slice along the Appalachian structural front. Tectonophysics 407 (3–4), 189–209.

Sibson, R.H., 1985. A note on fault reactivation. Journal of Structural Geology 7, 751–754.

Sibson, R.H., 2003. Thickness of the seismic slip zone. Bulletin of the Seismological Society of America 93 (3), 1169–1178.

Sharp, W.E., 1965. The deposition of hydrothermal quartz and calcite. Economic Geology 60 (8), 1635–1644.

Sharp, Z.D., 1990. A laser-based microanalytical method for the in situ determination of oxygen isotope ratios of silicates and oxides. Geochimica et Cosmochimica Acta 54 (5), 1353–1357.

Sharp, Z.D., Kirschner, D.L., 1994. Quartz-calcite oxygen isotope thermometry: a calibration based on natural isotopic variations. Geochimica et Cosmochimica Acta 58, 4491–4501.

Shiro, Y., Sakai, H., 1972. Calculation of the reduced partition function ratios of alpha–beta quartz and calcite. Japan Chemical Society Bulletin 45, 2355–2359.

Solum, J.G., van der Pluijm, B.A., 2009. Quantification of fabrics in clay gouge from the Carboneras fault, Spain and implications for fault behavior. Tectonophysics 475 (3–4), 554–562.

Sterner, S.M., Bodnar, R.J., 1984. Synthetic fluid inclusions in natural quartz, I. Compositional types synthesized and applications to experimental geochemistry. Geochimica et Cosmochimica Acta 48, 2659–2668.

Teixell, A., 1996. The Anso transect of the southern Pyrenees: basement and cover thrust geometries. Journal of the Geological Society 153, 301–310.

Teixell, A., 1998. Crustal structure and orogenic material budget in the west-central Pyrenees. Tectonics 17, 395–406.

Teixell, A., Durney, D.W., Arboleya, M.L., 2000. Stress and fluid control on décollement within competent limestone. Journal of Structural Geology 22 (3), 349–371.

Travé, A., Labaume, P., Calvet, F., Soler, A., 1997. Sediment dewatering and pore fluid migration along thrust faults in a foreland basin inferred from isotopic and elemental geochemical analyses (Eocene southern Pyrenees, Spain). Tectonophysics 282 (1–4), 375–398.

Travé, A., Labaume, P., Calvet, F., Soler, A., Tritlla, J., Buatier, M., Potdevin, J.L., Seguret, M., Raynaud, S., Briqueu, L., 1998. Fluid Migration during Eocene Thrust Emplacement in the South Pyrenean Foreland Basin (Spain): An Integrated Structural, Mineralogical and Geochemical Approach. In: Geological Society, London, Special Publications, vol. 134(1) 163–188.

Travé, A., Labaume, P., Vergés, J., 2007. Fluid systems in foreland fold-and-thrust belts: an overview from the southern Pyrenees. In: Lacombe, O., Lavé, J., Roure, F., Vergés, J. (Eds.), Thrust Belts and Foreland Basins. Springer, pp. 93–116.

Veizer, J., Ala, D., Azmy, K., Bruckschen, P., Buhl, D., Bruhn, F., Carden, G.A.F., Diener, A., Ebneth, S., Godderis, Y., Jasper, T., Korte, C., Pawellek, F., Podlaha, O.G., Strauss, H., 1999. $^{87}Sr/^{86}Sr$, $\delta^{13}C$ and $\delta^{18}O$ evolution of Phanerozoic seawater. Chemical Geology 161 (1–3), 59–88.

Vilasi, N., Swennen, R., Roure, F., 2006. Diagenesis and fracturing of Paleocene–Eocene carbonate turbidite systems in the Ionian Basin: the example of the Kelçyra area (Albania). Journal of Geochemical Exploration 89 (1–3), 409–413.

Vilasi, N., Malandain, J., Barrier, L., Callot, J.-P., Amrouch, K., Guilhaumou, N., Lacombe, O., Muska, K., Roure, F., Swennen, R., 2009. From outcrop and petrographic studies to basin-scale fluid flow modelling: the use of the Albanian natural laboratory for carbonate reservoir characterisation. Tectonophysics 474 (1–2), 367–392.

Wiltschko, D.V., Lambert, G.R., Lamb, W., 2009. Conditions during syntectonic vein formation in the footwall of the Absaroka Thrust Fault, Idaho-Wyoming-Utah fold and thrust belt. Journal of Structural Geology 31 (9), 1039–1057.

Zeyen, H., Fernandez, M., 1994. Integrated lithospheric modeling combining thermal, gravity, and local isostasy analysis: application to the NE Spanish geotransect. Journal of Geophysical Research 99 (18), 89–102.

Zhang, Y.G., Frantz, J.D., 1987. Determination of the homogenization temperatures and densities of supercritical fluids in the system $NaCl–KCl–CaCl_2–H_2O$ using synthetic fluid inclusions. Chemical Geology 64, 335–350.

Zhang, S., Tullis, T.E., 1998. The effect of fault slip on permeability and permeability anisotropy in quartz gouge. Tectonophysics 295 (1–2), 41–52.

Zhang, S., Tullis, T.E., Scruggs, V.J., 2001. Implications of permeability and its anisotropy in a mica gouge for pore pressures in fault zones. Tectonophysics 335 (1–2), 37–50.

Zheng, Y.-F., 1993. Calculation of oxygen isotope fractionation in hydroxyl-bearing silicates. Earth and Planetary Science Letters 120, 247–263.

Zheng, Y.F., 1999. Oxygen isotope fractionation in carbonate and sulfate minerals. Geochemical Journal 33, 109–126.